Rapid Solidification of Sn-Cu-Al Alloys for High-Reliability, Lead-Free Solder: Part I. Microstructural Characterization of Rapidly Solidified Solders

KATHLENE N. REEVE, STEPHANIE M. CHOQUETTE, IVER E. ANDERSON, and CAROL A. HANDWERKER

Particles of Cu_xAl_y in Sn-Cu-Al solders have previously been shown to nucleate the Cu_6Sn_5 phase during solidification. In this study, the number and size of Cu_6Sn_5 nucleation sites were controlled through the particle size refinement of Cu_xAl_y *via* rapid solidification processing and controlled cooling in a differential scanning calorimeter. Cooling rates spanning eight orders of magnitude were used to refine the average Cu_xAl_y and Cu_6Sn_5 particle sizes down to submicron ranges. The average particle sizes, particle size distributions, and morphologies in the microstructures were analyzed as a function of alloy composition and cooling rate. Deep etching of the samples revealed the three-dimensional microstructures and illuminated the epitaxial and morphological relationships between the Cu_xAl_y and Cu_6Sn_5 phases. Transitions in the Cu_6Sn_5 particle morphologies from faceted rods to nonfaceted, equiaxed particles were observed as a function of both cooling rate and composition. Initial solidification cooling rates within the range of 10^3 to 10^4 °C/s were found to be optimal for realizing particle size refinement and maintaining the Cu_xAl_y/Cu_6Sn_5 nucleant relationship. In addition, little evidence of the formation or decomposition of the ternary-β phase in the solidified alloys was noted. Solidification pathways omitting the formation of the ternary-β phase agreed well with observed room temperature microstructures.

I. INTRODUCTION

ALUMINUM micro-alloying additions have been shown to affect the solidification and microstructure of Pb-free solder alloys, particularly in Sn-Ag-Cu and Sn-Cu solder alloys, by reducing solder undercooling, eliminating or reducing the Ag_3Sn intermetallic compound (IMC) plate morphology, and forming Cu_xAl_y IMCs.[1–6] To form solder joints, solder alloys are commonly converted into powder particles, incorporated into a solder paste, and melted and solidified in final assembly to connect components to circuit boards. In the context of designing Sn-Cu-Al solder joint alloys, it is important to establish what the optimal Cu_xAl_y microstructures should be in both the as-fabricated powder and after soldering of the components is completed. Design factors that must be considered include:

1. The role of solidification cooling rate and alloy composition on the formation, morphologies, and size distributions of Cu_xAl_y particles
2. The ability of Cu_xAl_y to serve as a heterogeneous nucleation catalyst for the Cu_6Sn_5 IMC phase, and the resulting morphologies and sizes of the Cu_6Sn_5
3. The possible presence of the ternary-β phase during Sn-Cu-Al alloy solidification and its subsequent decomposition at low temperatures, as predicted by thermodynamics calculations, and its possible effect on Cu_6Sn_5 nucleation.[2,5,6]

Reeve *et al.* confirmed the initial formation of the Cu_xAl_y phases in the temperature ranges of 723 K to 823 K (450 °C to 550 °C) for seven different Sn-Ag-Cu-Al alloys and two different Sn-Cu-Al alloys.[2] The observation of this high solidification temperature provides the possibility of Cu_xAl_y IMC particles serving as persistent heterogeneous nucleation catalysts for the Cu_6Sn_5 phase, where "persistence" is defined as having minimal coarsening after multiple solder reflow cycles to a maximum temperature of 523 K (250 °C), as typically required for circuit board assembly. Xian *et al.* observed Cu_6Sn_5 formation on Cu_xAl_y particles within Sn-4.0Cu-xAl and Sn-0.7Cu-0.05Al wt pct alloys, and they identified the orientation relationship between the two IMC phases:[5,6]

KATHLENE N. REEVE, Ph.D. Candidate, and CAROL A. HANDWERKER, Reinhardt Schuhmann Jr. Professor, are with Purdue University, 701 West Stadium Ave., West Lafayette, IN 47907. Contact e-mail: klindley@purdue.edu STEPHANIE M. CHOQUETTE, Graduate Student, and IVER E. ANDERSON, Senior Metallurgist, are with the Ames Laboratory (USDOE), Iowa State University, Ames, IA 50011.

$$(1\bar{2}10)_{Cu_6Sn_5} \| (10\bar{1})_{Cu_xAl_y} \text{ and } [0001]_{Cu_6Sn_5} \| [111]_{Cu_xAl_y}$$

Xian *et al.* determined that for a Sn-4.0Cu-0.2Al wt pct alloy, the nucleation undercooling for the Cu_6Sn_5 IMC was reduced from 7.8 K to 3.6 K (-265.2 °C to -269.4 °C) and the number of Cu_6Sn_5 IMC grains per unit area increased by a factor of eight, as dictated by the number of Cu_xAl_y particles.[5] More recently, Xian *et al.* have shown the influence of dilute additions of Al on the formation of Cu_6Sn_5 in a Sn-0.7Cu-0.05Al wt pct alloy, where they noted that the number of primary Cu_6Sn_5 rose by a factor of seven, while the length of (rod-like) Cu_6Sn_5 particles was reduced by a factor of four, compared with a Sn-0.7Cu wt pct alloy.[6]

Some of the earliest assessments of the Cu-rich IMCs within the Cu-Al binary system were presented by Smith *et al.*[7] and by Wasserman.[8] An extensive review of the system and an updated binary phase diagram was given by Murray[9] and subsequently modified by Liu *et al.*[10] and Okamoto.[11] The most recent update to the Cu-Al binary was made by Ponweiser *et al.*[12] Notable shifts in phase fields were made for several Cu-rich IMCs, where the similarities between the crystal structures of $Cu_{33}Al_{17}$ (δ) and Cu_9Al_4 (γ) phases and the narrowing of the two-phase field between these two phases was analyzed.[12] Recent revisions have also been made to the Cu-Sn binary system, particularly in reference to the high-temperature, Cu-rich IMC β phase.[13,14]

In the ternary Sn-Cu-Al system, the phase diagram is incomplete. The similarities between the crystal structures and probable ranges of stoichiometry of the IMCs, the numerous morphological and compositional changes seen during the predicted ternary-β phase decomposition for multiple alloys, and the presence of a liquid–liquid miscibility gap have led to several plausible phase diagrams being proposed, but inconsistencies remain.[15–18] In a recent study, Chakrabarty and Jacob analyzed formation, stability, and decomposition of Cu-rich Sn-Cu-Al ternary alloys, observing the formation of α, β, γ, and the ordered β_1 ternary phases after long-term isothermal annealing of alloys between 773 K and 823 K (500 °C and 550 °C).[16,17] These results, as well as the results from Reeve *et al.* on Sn-rich alloys,[2] indicate that the alloy composition, the alloy liquid equilibration temperature (above or below the liquidus) before cooling begins, and the solidification path of the alloy are all extremely important factors in terms of the resulting room temperature solidification microstructure and the presence of ternary IMC phases within these Sn-Cu-Al alloys.

One question remaining for Sn-rich Sn-Cu-Al ternary alloys is whether the formation and subsequent solid-state decomposition of the ternary-β actually occurs, or whether the ternary-β phase is, in fact, unstable, contrary to the current thermodynamic predictions. Figure 1 displays the distinctly different types of solidification paths predicted for three different alloy compositions, with and without the formation of the ternary-β phase, and Figure 2 shows the computed Sn-Cu-Al ternary liquidus projection from the Sn-rich

corner, such that the IMC transitions can be viewed.[18] The presence, or absence, of the ternary-β phase during solidification of these alloys has a notable effect on the stability and formation of other IMC phases within the system. The room temperature stable phases within all of the compositions when the ternary-β phase is present during solidification are β-Sn, Cu_9Al_4 (γ_1), and Cu_6Sn_5 (η') (Figures 1(a) through (c)). When the ternary-β is omitted in the solidification predictions (Figures 1(d) through (f)), the room temperature stable phases within all three alloys become β-Sn, $Cu_{33}Al_{17}$ (δ), and Cu_6Sn_5 (η'). Additionally, the omission of the ternary-β phase from the solidification predictions has a major effect on the temperature stability and formation of Cu_6Sn_5 within all of the alloys. In all cases, suppression of the ternary-β phase increases the temperature stability of Cu_6Sn_5 through the formation of the hexagonal, high-temperature Cu_6Sn_5 (η) phase. Additionally, when the ternary-β phase formation is suppressed, as seen in Figures 1(d) through (f), a variation in temperature stability of the Cu_6Sn_5 formation, in reference to the typical solder reflow processing temperature of 523 K (250 °C) used during microelectronics fabrication, can be seen. Composition #1 (Figure 1(d)) displayed formation of Cu_6Sn_5 (η) directly at the ternary eutectic transition [500 K (227 °C)], composition #2 (Figure 1 (e)) displayed proeutectic formation of Cu_6Sn_5 (η) at ~513 K (~240 °C) [below the 523 K (250 °C) solder reflow processing temperature], and composition #3 (Figure 1(f)) displayed proeutectic formation of the Cu_6Sn_5 (η) at ~540 K (~267 °C) [above the 523 K (250 °C) solder reflow processing temperature]. Therefore, the formation of the ternary-β phase, although not stable at room temperature, has a notable influence over the predicted microstructure of the alloys and the temperature stability of the resulting phases.

In this article, we have used these three compositions to investigate the high-temperature stability and morphologies of the Cu_xAl_y phases as a function of composition and cooling rate, the nucleant relationship with Cu_6Sn_5, and the possible presence of the ternary-β phase during solidification *via* rapid solidification and controlled differential scanning calorimetric (DSC) cooling. The ability to dictate the formation, size, and size distribution of both the Cu_xAl_y and, subsequently, the Cu_6Sn_5 phase has the potential to not only improve solder joint uniformity but also to improve solder joint mechanical performance and fatigue tolerance. Xian *et al.* noted that the combination of constitutional supercooling in the liquid and the potent Cu_xAl_y nuclei resulted in the nucleation of Cu_6Sn_5 at a number density that was likely dependent on the size and distribution of the Cu_xAl_y IMC particles within the system.[5] In this article, these ideas have been tested by controlling the Cu_xAl_y and Cu_6Sn_5 phases through variations in composition and solidification cooling rate, from slow cooling to rapid solidification processing (RSP) and melt spinning. The resulting microstructures are analyzed in regard to both IMC phases present (Cu_xAl_y and Cu_6Sn_5), the resulting morphologies, the relative association between the IMC and the resulting IMC particle
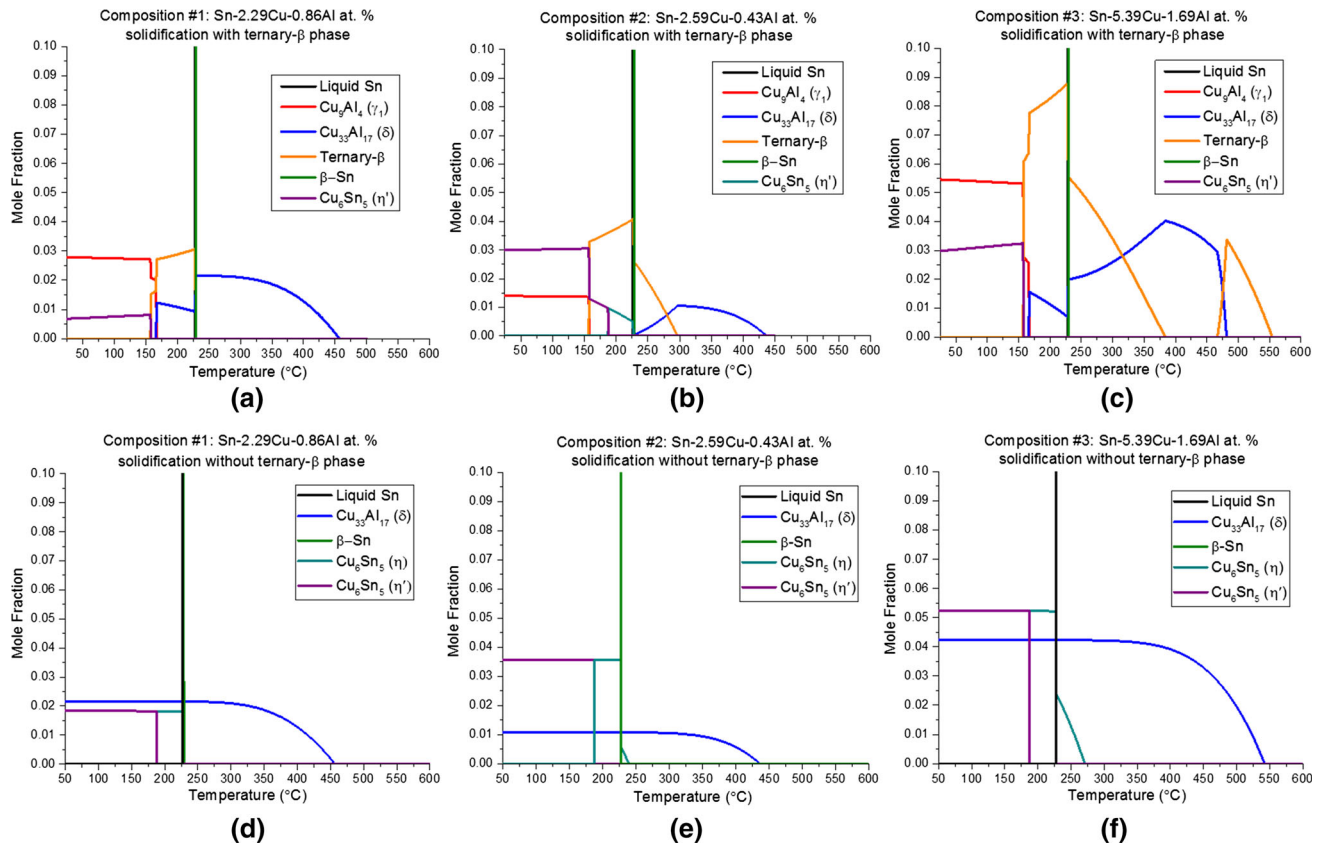
Fig. 1—Predicted alloy solidification paths (*a*) through (*c*) with the ternary-β formation and (*d*) through (*f*) without the ternary-β phase formation for all alloy compositions produced *via* Thermo-Calc TCSLD1. The y-axis of each diagram is magnified to show the transitions of the IMC phases at 0–0.1 mole fraction. (Color figures available online.) (http://www.thermocalc.com/start/—Thermo-Calc Software, Stockholm, Sweden.).
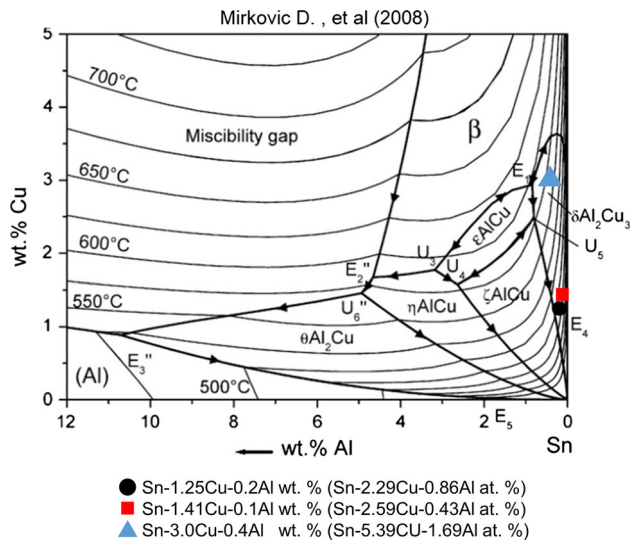

Fig. 2—Projection of the Sn-Cu-Al ternary liquidus surface. The presented figure has been adapted from Mirković *et al.* and orthogonally displays the Sn-rich corner of the ternary such that the transitions of the labeled sample compositions can be viewed.[18] (Color figures available online.).

sizes, the coarsening rates of the IMC, and the shifts in particle size distributions across the chosen cooling rate regimes.

II. EXPERIMENTAL VARIABLES AND PROCEDURES

Three different Sn-Cu-Al alloy compositions and four distinct cooling rate regimes resulted in estimated cooling rates that span eight orders of magnitude for Part I of this study. Table I outlines the cooling methods, the estimated cooling rates for each method, the alloy compositions of the samples used within each cooling method, and all of the collected and calculated particle data for the Cu_xAl_y and Cu_6Sn_5 phases.

(Note that the average IMC compositions, and hence, the dominant Cu_xAl_y phase ($Cu_{33}Al_{17}$ *vs* Cu_9Al_4), was determined by energy-dispersive spectroscopy (EDS), as described as follows.) Three alloy compositions were studied: #1—Sn-2.29Cu-0.86Al at. pct (Sn-1.25Cu-0.2Al wt pct), #2—Sn-2.59Cu-0.43Al at. pct (Sn-1.41Cu-0.1Al wt pct), and #3—Sn-5.39Cu-1.69Al at. pct (Sn-3.0Cu-0.4Al wt pct). These alloys allowed comparison of the effects of (1) different theoretical (maximum) volume fractions of the Cu_xAl_y and Cu_6Sn_5 IMC phases at room temperature, (2) different solidification pathways with respect to formation of the ternary-β IMC and Cu_6Sn_5 phases as predicted from thermodynamic calculations, and (3) different cooling rates on morphologies and spatial relationships between the various IMCs as they formed. Four cooling methods were chosen to study the effects of alloy cooling rate from a common superheat temperature of 1473 K (1200 °C) on the solder IMC

microstructure: controlled DSC cooling at the four different cooling rates of 0.017 °C/s (1 °C/min), 0.17 °C/s (10 °C/min), 0.83 °C/s (50 °C/min), and 1.65 °C/s (99 °C/min); ice water quenching (WQ) (estimated cooling rate of 10^3 °C/s); drip atomization (DA) of 260-μm-diameter spheres (estimated cooling rate of 10^4 °C/s); and melt spinning at two different wheel speeds, 5 and 25 m/s, (estimated cooling rates of 10^5 and 10^6 °C/s, respectively). The common superheat temperature of 1473 K (1200 °C) was chosen specifically to ensure solidification from a homogeneous alloy liquid, as it was previously shown by Reeve et al. that variations in superheat temperature [1473 K vs 1073 K (1200 °C vs 800 °C)] can have a notable effect on the as-solidified Cu_xAl_y particle size.[2] All of the as-solidified solder samples were then analyzed via scanning electron microscopy (SEM). It must be noted that measuring of solidification rates for specific RSP methods is still an area of debate within the field.[19] Accurately measuring the temperature of a rapidly cooled melt, estimating the heat transfer coefficients for various heat sinks, and assessing the nucleation temperature of an alloy all present difficulties for the determination of rapid solidification rates. Due to these well-known issues, the authors have assigned cooling rates to specific RSP methods based on conventional order-of-magnitude estimates.

A. DSC Controlled Cooling

The DSC cooled samples were prepared from elemental Sn, Cu, and Al of 99.99 pct purity at the Materials Preparation Center (MPC) of Ames Laboratory.*

---

*Ames Laboratory Materials Preparation Center, Ames, IA, USA. http://www.ameslab.gov/mpc.

The original alloy casting from which the DSC samples were prepared was made via the same procedure as described for the WQ samples, with length of wire (1.7 mm diameter) drawn from the WQ ingot. A 100-mg sample was cut from the wire for each DSC slow cooling rate experiment. The DSC employed was a Pegasus heat flux DSC 404C by Netzch. Each sample was placed in an alumina crucible, continually flushed with nitrogen, and heated to a superheat of 1473 K (1200 °C) at 20 °C/min (0.33 °C/s). Each sample was held at the 1473 K (1200 °C) superheat temperature for 10 minutes and cooled at the specified cooling rates of either 0.017, 0.17, 0.83, or 1.65 °C/s. Two alloy samples (~100 mg) were run through the DSC slow cooling rate procedure per cooling rate. Each sample cross section was then analyzed, resulting in two cross sections examined per the four different cooling rate procedures. Figure 1(d) shows the predicted solidification path for the Sn-2.29Cu-0.86Al at. pct alloy (composition #1) chosen for the DSC cooled samples. The room temperature microstructure was predicted to be composed of three phases, β-Sn + Cu_6Sn_5 (η') + $Cu_{33}Al_{17}$ (δ).

B. Ice Water Quenching

The WQ samples were prepared from elemental Sn, Cu, and Al of 99.99 pct purity at the Materials Preparation Center (MPC) of Ames Laboratory. The castings were made as 100g samples, sealed in quartz tubes under an argon atmosphere,

superheated at 1473 K (1200 °C) for 60 minutes (with periodic agitation), and finally quenched into an ice water bath with no fracture of the quartz tube ampule. The solder ingots were then drawn into 1.7-mm-diameter wires, from which the samples were cut for microstructural examination. Wire drawing was used to homogenize the microstructure. One longitudinal wire cross section (~2 cm long) and one transverse wire cross section (0.17 cm) were characterized for each of the two different WQ sample compositions (Sn-2.29Cu-0.86Al and Sn-5.39Cu-1.69Al at. pct) shown in Table I. Figures 1(d) and (f) display the predicted solidification paths for the Sn-2.29Cu-0.86Al at. pct (composition #1) and Sn-5.39Cu-1.69Al at. pct (composition #3) alloys chosen for the WQ cooled samples. The room temperature microstructures were predicted to be composed of three phases, β-Sn + Cu_6Sn_5 (η') + $Cu_{33}Al_{17}$ (δ).

C. Drip Atomization

The target composition of the DA ball grid array (BGA) spheres was Sn-2.59Cu-0.43Al at. pct (Sn-1.41Cu-0.10Al wt pct). To produce the desired alloy composition, the following masses were added to an Ar-filled graphite crucible: 984.9 g of elemental Sn, 7.1 g of elemental Cu, and 8.0 g of a Cu-Al master alloy, with a final composition targeted to produce $Cu_{33}Al_{17}$ (δ) IMC in a Sn-Cu alloy. To initially alloy in the added materials, the crucible was heated to 1073 K (800 °C) and held for 15 minutes. The temperature of the crucible was then increased to 1473 K (1200 °C) and held for 10 minutes. The alloyed liquid was DA processed with a proprietary system (Fukuda Co.) that used a pulsating plunger to force the alloy melt through an orifice plate, resulting in 260-μm-diameter spheres. The spheres were cooled and solidified during free-fall in an inert argon gas chamber. Clogging of the crucible occurred prematurely after 10 minutes of atomization, yielding a final efficiency of 0.2 pct of the starting alloyed melt. The drip atomization was performed by Fukuda Co. in Japan,** facilitated by Nihon

---

**Fukuda Metal Foil and Powder Co., Yamashina-ku, Kyoto, Japan. http://www.fukuda-kyoto.co.jp/01info-e/f-kyoten.html.

Superior.†Cross sections of ten different DA spheres were

---

†Nihon Superior, Esaka-Cho, Suita City, Osaka, Japan. http://www.nihonsuperior.co.jp/english/.

---

characterized by SEM/EDS analysis of the alloy. Figure 1(e) shows the predicted solidification path for the Sn-2.59Cu-0.43Al at. pct alloy (composition #2) chosen for the drip atomization. The room temperature microstructure was predicted to be composed of three phases, β-Sn + Cu_6Sn_5 (η') + $Cu_{33}Al_{17}$ (δ).

D. Melt Spinning

Two melt spun ribbon (MSR) alloy castings were produced via the melt spinning operation, both with a

Table I. Cooling Methods, Estimated Cooling Rates, Sample Compositions, Cu_xAl_y Particle Data, and Cu_6Sn_5 Particle Data for All Samples

Cooling Method	Estimated Cooling Rate (°C/s)	Sample Composition (at. pct)			Cu_xAl_y Particle Data					Cu_6Sn_5 Particle Data							
		Sn	Cu	Al	Unimodal Avg. Dia. (μm)	Max. Dia. (μm)	Min. Dia. (μm)	Avg. Vol Pct	Calc. Vol Pct	Unimodal Avg. Dia. (μm)	Bimodal Avg. Dia. (μm)	Max. Dia. (μm)	Min. Dia. (μm)	Avg. Aspect Ratios	Avg. Vol pct	Calc. Vol pct	Morphology
DSC	0.017	96.84	2.29	0.86	93 ± 28	133	56	—	1.19	9.1 ± 4.8	2.3 ± 1.5 79 ± 37*	245	0.4	1.7 ± 0.9	—	0.59	faceted (hollow core)
DSC	0.17	96.84	2.29	0.86	60 ± 15	84	27	—	1.19	1.2 ± 0.1	1.8 ± 1.0 11 ± 2.1	8.9	0.4	1.5 ± 0.6	—	0.59	—
DSC	0.83	96.84	2.29	0.86	39 ± 7.4	53	23	—	1.19	2.7 ± 2.1	2.0 ± 1.5 31 ± 17	56	0.4	1.8 ± 1.1	—	0.59	faceted (hollow core)
DSC	1.65	96.84	2.29	0.86	31 ± 11	52	10	—	1.19	4.8 ± 3.1	—	132	0.4	2.0 ± 1.2	—	0.59	faceted (hollow core)
WQ	10^3	96.84	2.29	0.86	5.4 ± 2.4	17	1.4	1.2 ± 0.5	1.19	0.6 ± 0.4	—	3.1	0.1	1.3 ± 0.4	0.6 ± 0.2	0.59	non-faceted
DA	10^4	96.97	2.59	0.43	0.5 ± 0.2	2.3	0.02	0.6 ± 0.1	0.59	0.6 ± 0.3	—	4.8	0.04	1.8 ± 1.2	1.2 ± 0.2	1.22	faceted (start of hollow core)
WQ	10^3	92.92	5.39	1.69	3.6 ± 2.0	11	1.0	2.0 ± 0.5	2.39	2.5 ± 2.0	—	8.9	0.2	1.5 ± 0.5	2.2 ± 0.6	1.90	faceted (hollow core)
MSR	10^5	92.92	5.39	1.69	0.1 ± 0.1	1.0	0.01	2.1 ± 1.3	2.39	0.5 ± 0.4	—	2.7	0.05	1.6 ± 0.7	2.1 ± 0.6	1.90	non-faceted
MSR	10^6	92.92	5.39	1.69	0.1 ± 0.1	0.8	0.01	2.3 ± 0.6	2.39	0.3 ± 0.2	—	2.4	0.03	1.5 ± 0.5	1.7 ± 0.6	1.90	non-faceted

*Single outlier excluded (245 μm) from calculation of average and standard deviation.

target composition #3. The melt-spinner, located at Ames Laboratory, was housed in a custom stainless steel vacuum chamber. The rotating chill block that acted as the heat sink for the alloy melt during the RSP was made of oxygen-free high-conductivity (OFHC) copper. The chill block was rotated at chill surface speeds of 5 and 25 m/s to produce two different cooling rates for the two separate cast ribbons. Differential pressure for melt ejection was measured by means of a differential pressure manometer and was set at 105 torr (~2 psi). The crucible material that held the alloy melt was a SiO_2 (quartz glass) with an outer diameter of 15 mm. The orifice diameter of the crucible was 0.8 mm and was formed by use of an embedded quartz precision capillary. The heating of the alloy was performed with a Pillar 15 kW 450-kHz induction generator and during casting each melt was superheated to 1473 K (1200 °C), as monitored by a two-color pyrometer. Upon release of the molten alloy and impingement with the rotating copper chill block, rapidly solidified cast ribbons were formed. Estimated cooling rates for the two alloy cast ribbons were approximated to be 10^5 °C/s for the 5m/s chill block wheel speed and 10^6 °C/s for the 25-m/s wheel speed. Longitudinal cross sections of the ribbons (~2 cm long) were used for SEM analysis for each of the two different cool rate samples. Figure 1(f) shows the predicted solidification path for composition #3, chosen for the MSR samples. The room temperature microstructure is predicted to be composed of three phases, β-Sn + Cu_6Sn_5 (η') + $Cu_{33}Al_{17}$ (δ).

E. Metallography, SEM, and Particle Analysis

For microstructural analysis after each cooling rate treatment, the samples were metallographically cross sectioned and analyzed *via* SEM. The solder samples were mounted individually in a cold mount epoxy/resin and cured for 24 hours at room temperature. The sample surfaces were polished *via* a standard metallographic grinding and polishing sequence of 400/600/800/1200 grit SiC paper with water as a lubricant, followed by 1/0.5/0.25/0.05-μm diamond/glycol polishing suspension on high matte polishing pads (used specifically for soft metallic materials) with RedLube™ lubricant obtained from Allied High Tech Products Inc.[‡]In

---

[‡]Allied High Tech Products Inc, Rancho Dominquez, CA, USA. http://alliedhightech.com/.

---

addition to the standard metallographic sample preparations and two-dimensional (2-D) microstructural analysis *via* SEM, the WQ samples, DA sample, and MSR samples were deep etched and analyzed *via* SEM. The deep etching procedure employed was identical to the procedure outlined in Reference 20 and was used to etch away the β-Sn matrix phase for three dimensional (3-D) examination of the IMC morphologies present in the samples.

SEM images for the DSC cooled samples and for the WQ samples were obtained in backscatter electron

(BSE) mode at 20 keV on a Hitachi S-2460N SEM. SEM images for the WQ, DA, and MSR samples were gathered in BSE mode at 15 keV on a NanoScience Phenom Desktop—CeB$_6$ filament SEM. SEM images for the deep-etched DA sample were gathered in secondary electron (SE) mode at 5 keV on a FEI Quanta-250 Field Emission SEM at Iowa State University's Materials Analysis and Research Laboratory (MARL) microscopy facility.§

SEM images for deep etched WQ and MSR samples were obtained in both BSE and SE modes at 10 to 20 keV on a FEI Quanta 3-D Field Emission Dual-beam SEM at the Purdue Life Science Microscopy Facility (LSMF).§§

Finally, quantitative metallographic analysis was performed on the images with the use of ImageJ photo analysis software, freely available from NIH.¶

Particle size diameters, particle size distributions, and volume fractions for the Cu_xAl_y and Cu_6Sn_5 phases were measured *via* use of the ImageJ software particle analysis toolkit. Measurements *via* EDS were made throughout the analysis of all of the samples when the measurements could be reliably made on the Cu_xAl_y and Cu_6Sn_5 IMC. Due to the extremely small particle size of the Cu_xAl_y IMC within the MSR samples, no EDS measurements could be accurately made and therefore no EDS data regarding the Cu_xAl_y phase within the two MSR samples is given within this study.

III. RESULTS AND DISCUSSION

In these experiments, it was expected that IMC particle size would decrease with an increase in cooling rate. Additionally, it was predicted that one or both of the expected IMC phases, Cu_xAl_y and Cu_6Sn_5, within the system would exhibit morphological changes with variations in sample composition and cooling rate, possibly transitioning between faceted and nonfaceted morphologies. Such refinement of IMC particle size and changes in IMC morphology with increases in cooling rate and with variations in alloy chemistry occur across many metallurgical systems. To the authors' knowledge, no work has previously reported these phenomena within a Pb-free solder system in which both Cu_xAl_y and Cu_6Sn_5 IMC phases, given their identified nucleant relationship, were formed under the range of imposed solidification conditions. This section presents (1) how the Cu_xAl_y and Cu_6Sn_5 IMC initially form under the influence of increasing cooling rate conditions, (2) how the IMC particles interact under the various cooling rate conditions, and (3) how the IMC particle formation and interaction is influenced by alloy composition. The microstructural data are analyzed as follows for each composition in terms of resulting Cu_xAl_y and Cu_6Sn_5 IMC particle sizes, particle size distributions, compositions, morphologies, and degree of association between the two IMC phases. The results will then be summarized across the alloy compositions and cooling rate regimes in terms of overall IMC particle size refinement and the ideal solidification cooling rates for achieving simultaneous IMC particle size refinement and maintained preferred nucleation of Cu_6Sn_5 from the Cu_xAl_y surfaces. Throughout the results, it will be noted that there were very few IMC particles displaying possible ternary-β phase decomposition. Thus, the solidification paths omitting the formation of the ternary-β phase (Figures 1(d) through (f)) will be used from this point forward to discuss the presented sample microstructures. It was the variation in Cu_6Sn_5 temperature stability across the sample compositions that motivated the choice of the three Sn-Cu-Al alloys analyzed within this study (Figure 1(d) through (f), Table I). (Note that the difference in stability of the Cu_6Sn_5 phase for these alloys will also be important during Part II of this study, where the coarsening of both IMC phases during solder reflow cycling is analyzed.[21])

A. DSC Cooling and WQ Samples—Composition #1 (Sn-2.29Cu-0.86Al at. pct)

Particle size and volume fraction data are shown in Table I. The DSC and WQ samples showed formation of both Cu_xAl_y and Cu_6Sn_5 IMC with the average particle sizes showing a steady decrease in size with an increase in cooling rate. Undercooling within the DSC cooled samples ranged from 11 °C (0.017 °C/s cooling rate) to 8.5 °C (0.83 and 1.65 °C/s cooling rates). Undercooling for the WQ sample was recorded at approximately 8 °C, after casting and subsequent reflow of the cast sample at 1473 K (1200 °C) in the DSC.[2] Representative micrographs of the Sn-2.29Cu-0.86Al at. pct DSC and WQ samples can be seen in Figures 3(a) through (g). Compositional measurements made *via* EDS for both the Cu_xAl_y and Cu_6Sn_5 phases are shown in Table II. The micrographs of the DSC cooled samples in Figures 3(a) through (d) showed that all of the Cu_xAl_y particles were found along the outer edges of the as-solidified solder spheres. This was not observed for the Cu_6Sn_5 particles, which were found within the bulk. In contrast to faster cooling rates, where the solidification front likely entrapped Cu_xAl_y particles, larger Cu_xAl_y particles were likely pushed ahead of the Sn solidification front in the DSC cooled samples and thus were found only along the outer edges of the solder spheres. Buoyancy differences between the Cu_xAl_y phase and the Sn-liquid may also have contributed to their presence at the surface of the samples.[1]
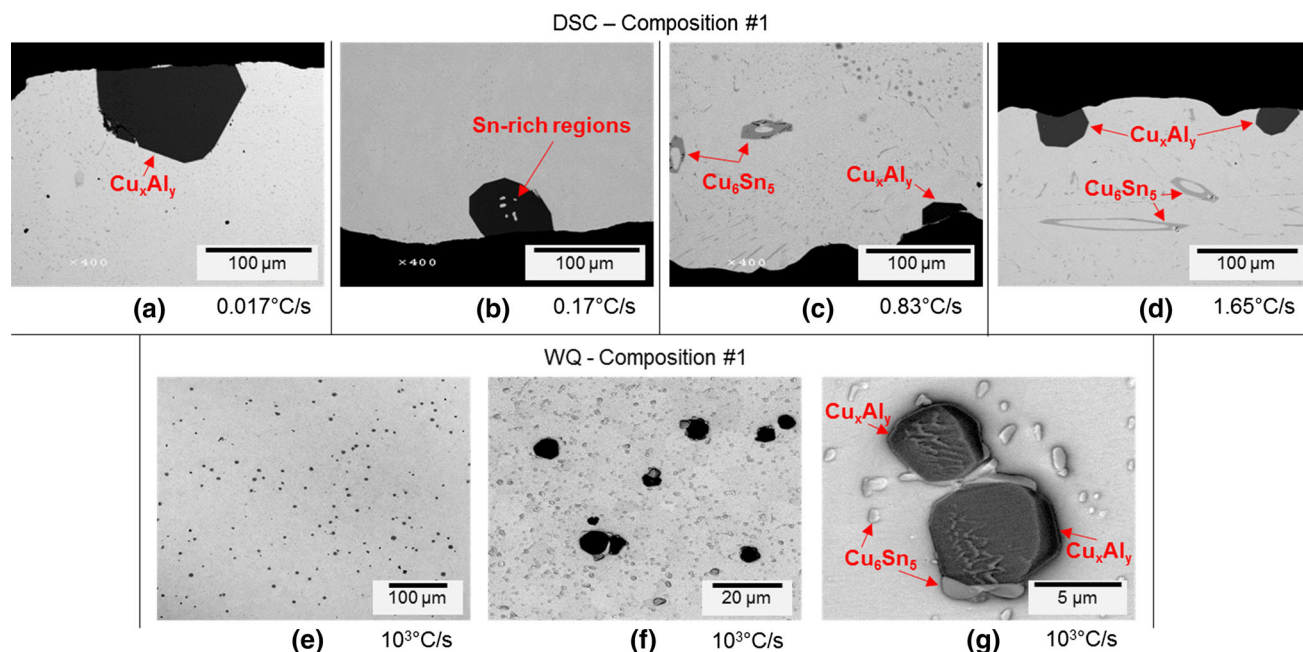
Fig. 3—Backscatter electron (BSE) SEM micrographs of the solder microstructures for the (*a*) through (*d*) DSC and (*e*) through (*g*) WQ composition #1 samples. The black contrast particles are Cu_xAl_y IMC, the dark gray contrast particles and areas are Cu_6Sn_5 IMC, and the light gray matrix is β-Sn. In (*a*) through (*d*), the black border along the β-Sn matrix is the edge of the DSC solder samples. (Color figures available online.).

Table II. Measured EDS Compositions for the Cu_xAl_y and Cu_6Sn_5 Phases Found Within the Sn-Cu-Al Solder Samples

Cooling Method	Est. Cooling Rate (°C/s)	Sample Compositions			EDS on Cu_xAl_y		EDS on Cu_6Sn_5		
		Sn	Cu	Al	Cu	Al	Cu	Sn	Al
DSC	0.017	96.84	2.29	0.86	68.1	32.0	52.2	47.1	—
DSC	0.17	96.84	2.29	0.86	66.8	33.2	—	—	—
DSC	0.83	96.84	2.29	0.86	68.8	31.3	50.6	48.7	—
DSC	1.65	96.84	2.29	0.86	67.5	32.4	50.5	48.9	—
WQ	10^3	96.84	2.29	0.86	63.0	34.4	54.4	45.6	—
DA	10^4	96.97	2.59	0.43	67.7	31.9	60.1	39.9	—
WQ	10^3	92.92	5.39	1.69	66.8	31.6	51.9	47.5	—
MSR	10^5	92.92	5.39	1.69	—	—	46.8	43.7	9.5
MSR	10^6	92.92	5.39	1.69	—	—	42.1	47.6	10.3

Accurate compositional measurement of the Cu_6Sn_5 within the 0.17 °C/s sample cross sections could not be made without the influence of the surrounding Sn matrix, and the Cu_xAl_y particle size within the MSR samples were too small for accurate EDS measurement (EDS spot size = 1 μm).
*All values are given in units of atomic percent (at. pct), unless otherwise stated.

For the DSC cooled samples, the slowest cooling rate (0.017 °C/s) had an average Cu_xAl_y particle diameter of 93 ± 28 μm, while the fastest cooling rate (1.65 °C/s) displayed an average Cu_xAl_y particle diameter of 31 ± 11 μm. In comparison, the WQ sample (10^3 °C/s) had an average measured Cu_xAl_y particle size of 5.4 ± 2.4 μm. It is useful to note that although there are few particles within the DSC samples, coarsening of the particles at these slower cooling rates was apparent. The large standard deviations for the measured average Cu_xAl_y particle diameters from the DSC samples was indicative of the small number of Cu_xAl_y IMC particles found

within the samples, with as few as two Cu_xAl_y particles found for the 0.017 °C/s samples. Particle size (diameter) distributions of the Cu_xAl_y phase as a function of cooling rate in Figures 4(a) through (e) show that the distribution narrows significantly as the cooling rate increases, from 56 to 133 μm for the 0.017 °C/s sample to 1.4 to 17 μm for the WQ (10^3 °C/s) sample. The average volume fraction of the Cu_xAl_y IMC was measured within the WQ sample to be 1.2 ± 0.5 pct, which is statistically the same as the theoretical volume fraction for Cu_xAl_y IMC of 1.19 pct. The Cu_xAl_y volume fractions within the DSC sample could not be accurately measured due to the small number of
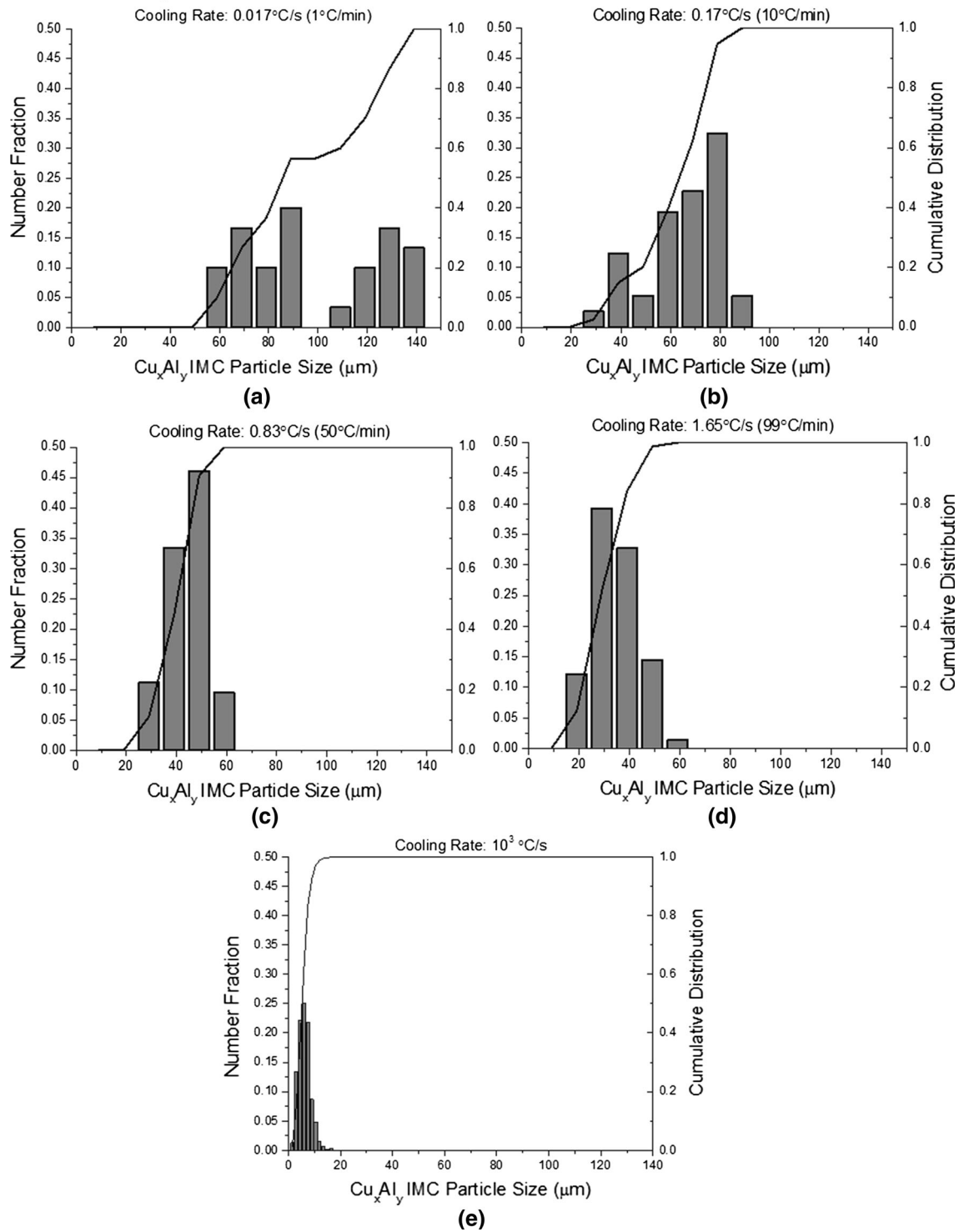
Fig. 4—(a) through (e) Cu$_x$Al$_y$ IMC particle size distributions for composition #1 DSC and WQ cooling rate samples. The y-axis shows the number fraction of Cu$_x$Al$_y$ particle (bars; left axes), as well as the cumulative distribution function (lines; right axes). The x-axis plots the Cu$_x$Al$_y$ IMC particle size.

Cu$_x$Al$_y$ particles within a given cross section. The morphology of the Cu$_x$Al$_y$ phase for this alloy was faceted for all applied cooling rates, 0.017 to 10^5 °C/s. Figures 5(a) through (d) shows images of the deep etched composition #1 WQ sample (10^5 °C/s) along

with qualitative EDS maps of the 2-D and 3-D surfaces of the WQ sample. In these images, the distribution of Sn, Cu, and Al within the microstructure can be seen, and the association of the Cu$_6$Sn$_5$ (η') phase with the surfaces of the Cu$_x$Al$_y$ phase is shown.
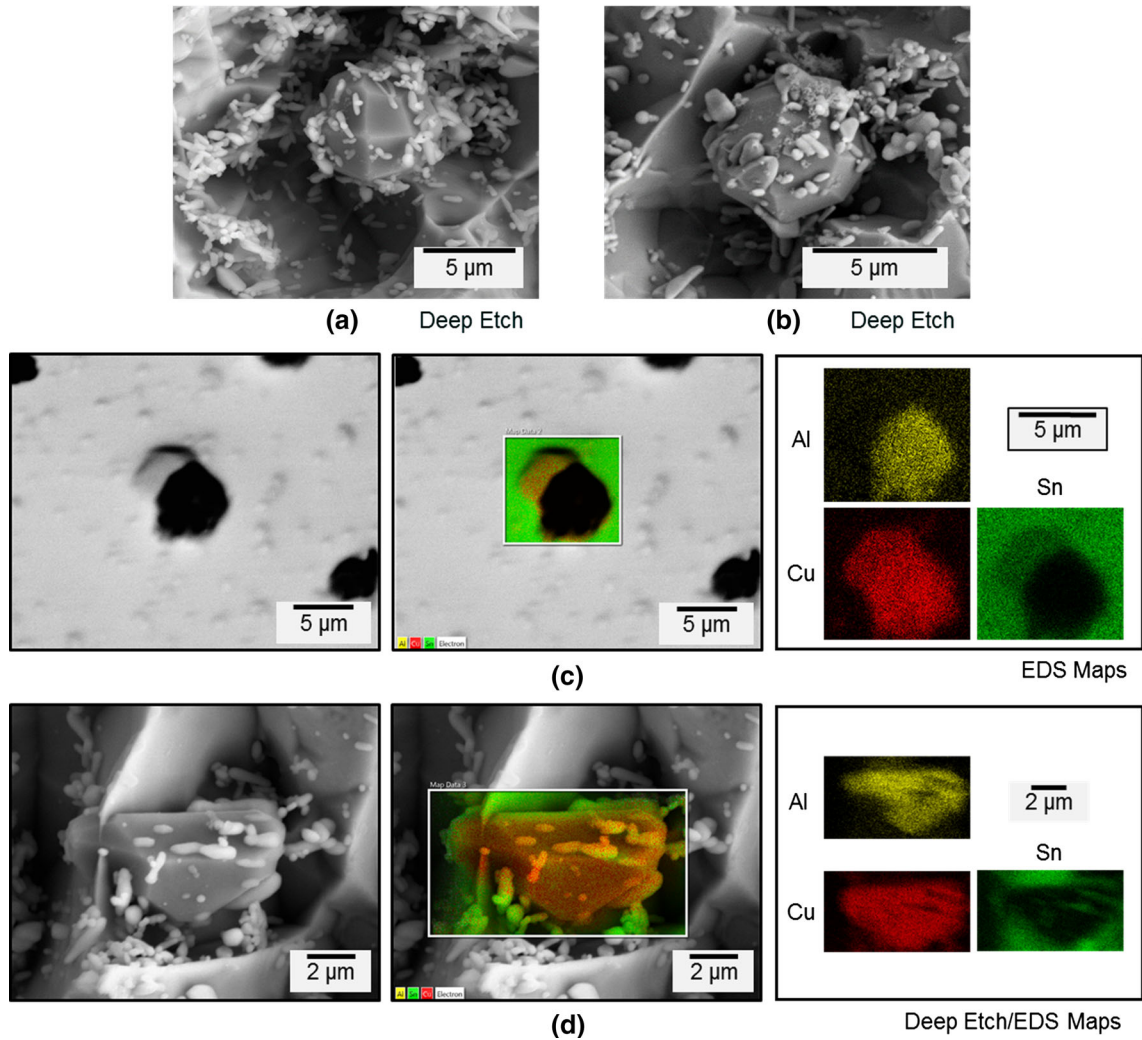
Fig. 5—(a) and (b) SEM secondary electron (SE) images of regions of Sn-2.29Cu-0.86Al at. pct WQ sample after deep etching to reveal the 3-D structure of the IMC within the alloy. (c) SEM EDS map scan of a 2-D cross section of the Sn-2.29Cu-0.86Al at. pct WQ sample taken in BSE mode, and (d) SEM EDS map of a 3-D structure of the Sn-2.29Cu-0.86Al at. pct WQ sample after deep etching taken in SE mode. Association between the Cu_6Sn_5 (light gray) and Cu_xAl_y (BSE = black, SE = dark gray) particle phases can be seen throughout the micrographs. (Color figures available online.).

The average Cu_xAl_y compositions measured *via* EDS for the DSC cooled samples indicated Cu and Al concentrations of 66.8–68.8 and 31.3–33.2 at. pct, respectively, with no detectable Sn, as seen in Table II. These average Cu_xAl_y compositions are all within the Cu_9Al_4 (γ_1) phase field.[12] The presence of the Cu_9Al_4 (γ_1) phase disagrees with the calculated room temperature microstructure for this alloy composition when omitting the ternary-β phase formation (Figure 1(d)). The average Cu_xAl_y composition in the WQ sample was 63.0 at. pct Cu and 34.4 at. pct Al, placing the WQ IMC composition within the $Cu_{33}Al_{17}$ (δ) phase field. The calculated solidification path for composition #1 (Figure 1(d)) predicts that the $Cu_{33}Al_{17}$ (δ) phase should be the first phase to form at ~723 K (~450 °C) in equilibrium with the Sn-liquid until the ternary eutectic where the alloy enters the three-phase field, *i.e.*, $Cu_{33}Al_{17}$ (δ) + Cu_6Sn_5 (η) + β-Sn. At ~462 K (~189 °C) the Cu_6Sn_5 (η) phase is predicted to decompose into the Cu_6Sn_5 (η') phase in the solid state, leaving three-phase equilibrium between β-Sn + Cu_6Sn_5 (η') + $Cu_{33}Al_{17}$ (δ). The EDS composition of the Cu_xAl_y particles within the DSC samples conflicts with the predicted room temperature microstructure, but it is noted that the exact phase boundary and existence of a two-phase region between the Cu_9Al_4 and $Cu_{33}Al_{17}$ phases within the binary diagram is still under debate,[12] and there is little difference that exists between the crystal structures of the two phases, primitive cubic ($\alpha = \beta = \gamma = 90°$)[22] and rhombohedral ($\alpha = \beta = \gamma = 89.74°$)[23] gamma brass structures, respectively.

For all but two Cu_xAl_y particles observed in this alloy, the Cu-Al IMC particles appeared to be single phase with convex surfaces. Two particles were observed that indicated possible decomposition of the ternary-β phase within composition #1 in this study but with different
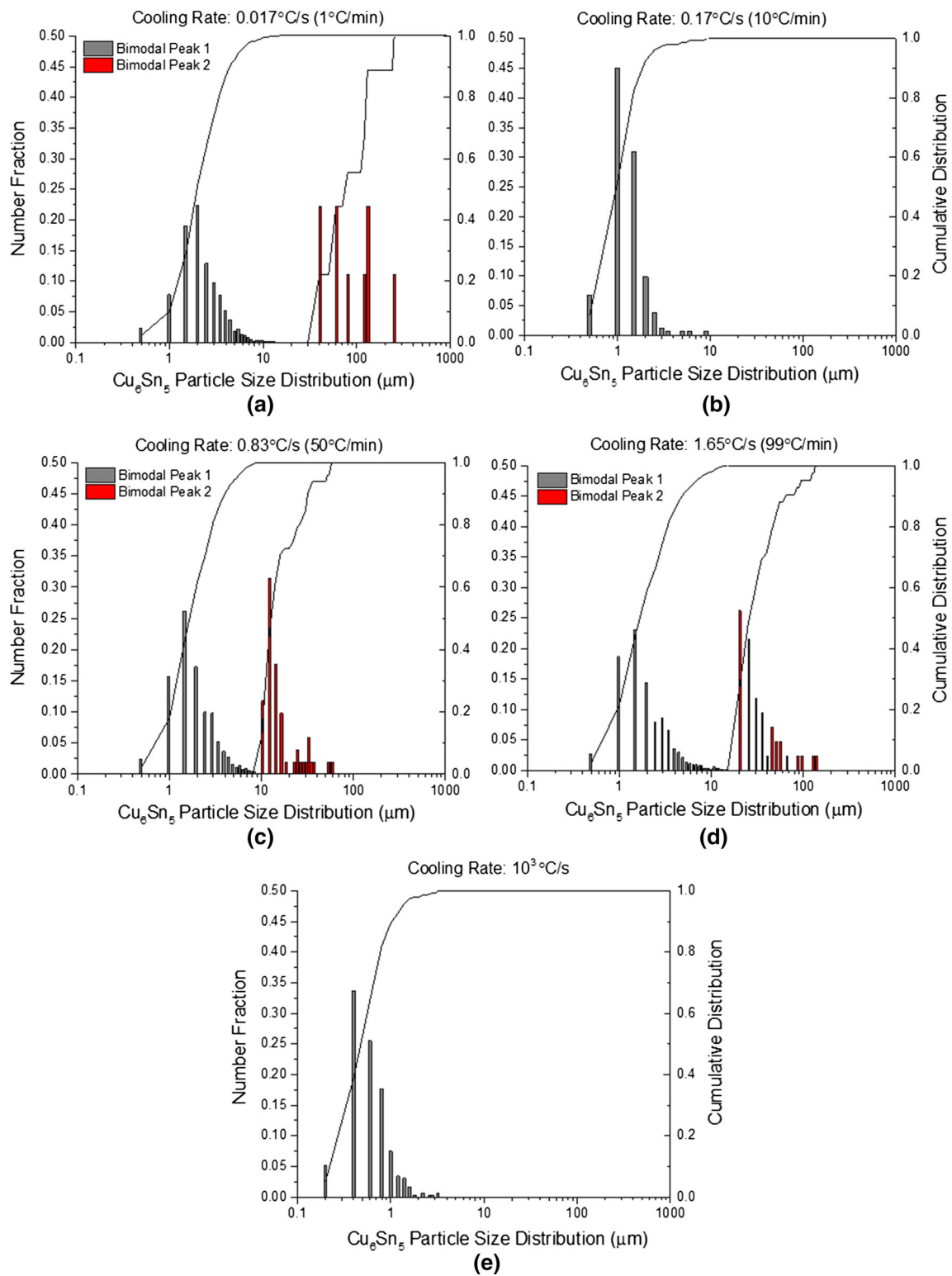
Fig. 6—(*a*) through (*e*) Cu$_6$Sn$_5$ IMC particle size distributions for the Sn-2.29Cu-0.86Al at. pct DSC and WQ cooling rate samples. The y-axis show the number fraction of Cu$_6$Sn$_5$ particles (bars, left axes) as well as the cumulative distribution function (lines, right axes). The x-axis plots the Cu$_6$Sn$_5$ IMC particle size in log scale for 0.1 to 1000 *μ*m. (Color figures available online.).

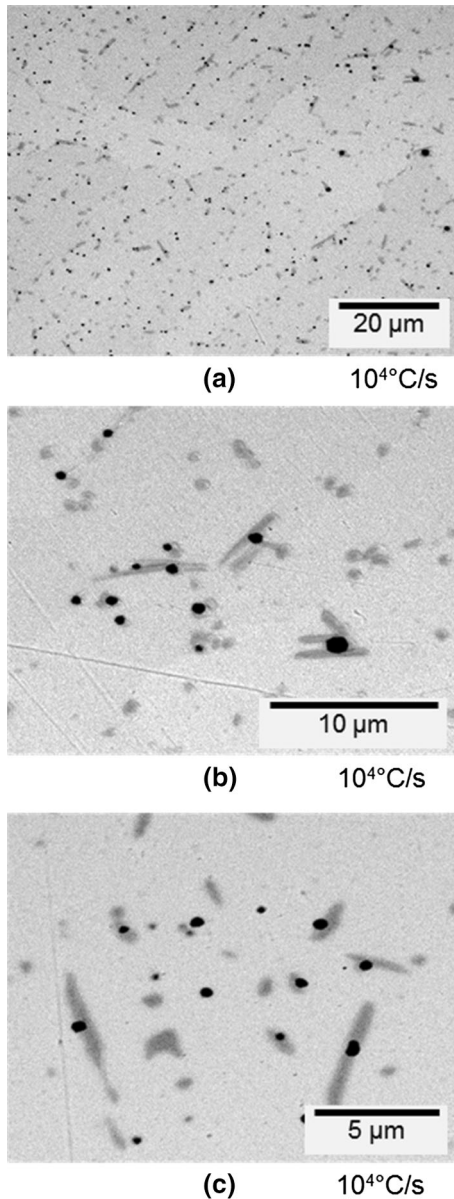**(a)** 10⁴°C/s

(b) 10⁴°C/s

(c) 10⁴°C/s

Fig. 7—(*a*) through (*c*) BSE SEM micrographs of the solder microstructure for DA Sn-2.59Cu-0.43Al at. pct sample (10^4 °C/s). The black contrast particles are Cu$_x$Al$_y$ IMC, the dark gray contrast particles and areas are Cu$_6$Sn$_5$ IMC, and the light gray matrix is β-Sn.

decomposition reactions. The 0.17 °C/s sample (Figure 3(b)) showed entrapped Sn-rich regions within a Cu$_9$Al$_4$ particle; in contrast, the WQ (10^3 °C/s) sample showed Cu-rich regions within one observed Cu$_{33}$Al$_{17}$ particle (shown in Reference 2 in Figure 4(a)). The Sn-rich regions within the Cu$_9$Al$_4$ particle in the 0.17 °C/s sample had a measured EDS composition of 89.3Sn-9.6Cu at. pct, with contribution of Cu signal likely from the surrounding Cu$_9$Al$_4$ phase due to the small size of the Sn-rich regions. The Cu-rich regions within the Cu$_{33}$Al$_{17}$ particle in the WQ (10^3 °C/s) sample had an average EDS composition of 78.2Cu-20.6Al-1.0Sn at. pct, which was close to the equilibrium composition found for the α phase by Chakrabarty and Jacob.[17] There

were no other observed microstructural features that indicated possible decomposition of the ternary-β or β$_1$ phases within this set of samples.

The IMC particle data for Cu$_6$Sn$_5$ are also shown in Table I. The slowest DSC cooling rate of 0.017 °C/s produced the largest Cu$_6$Sn$_5$ particles, with a unimodal average of 9.1 ± 4.8 *μ*m and bimodal particle size averages of 2.3 ± 1.5 and 79 ± 37 *μ*m, with the lower peak in the distribution likely representing the eutectic formation of the phase and the higher peak representing the primary formation of the phase. The 0.17 °C/s cooling did not produce any primary Cu$_6$Sn$_5$ within the sample cross sections and displayed only eutectic formation with a unimodal average particle size of 1.2 ± 0.1 *μ*m. The DSC cooling rates of 0.86 and 1.65 °C/s produced bimodal Cu$_6$Sn$_5$ particle size distributions, with averages of 1.8 ± 1.0 and 11 ± 2.1 *μ*m, and 2.0 ± 1.5 and 31 ± 17 *μ*m, respectively. The average Cu$_6$Sn$_5$ particle size for the WQ (10^3 °C/s) sample was measured at 0.6 ± 0.4 *μ*m. The particle size distributions for the Cu$_6$Sn$_5$ phase can be seen in Figures 6(a) through (d). It can be seen from the distributions in Figures 6(a) through (d) that the Cu$_6$Sn$_5$ particle size narrows as the cooling rate of the samples increases, from 0.4 to 245 *μ*m in the 0.017 °C/s sample to 0.1 to 3.1 *μ*m in the WQ (10^3 °C/s) sample. The average volume fraction of the Cu$_6$Sn$_5$ phase within the WQ sample was measured at 0.6 ± 0.2 pct, which is in good agreement with the 0.59 pct calculated for the theoretical volume fraction of the Cu$_6$Sn$_5$ for this alloy at room temperature. No volume fraction values were determined for the DSC samples due to the small number of Cu$_6$Sn$_5$ particles within the samples.

The EDS measurements from the Cu$_6$Sn$_5$ phase within the DSC cooled samples revealed Cu and Sn concentrations ranging from 50.5 to 52.2 and from 47.1 to 48.9 at. pct, respectively, placing the phase composition near that of the Cu$_6$Sn$_5$ (η′) phase, but slightly Cu-poor, within the Cu$_6$Sn$_5$ (η′) + β-Sn two phase. The measured Cu and Sn concentrations had Cu:Sn ratios ranging from 1.03 to 1.11, while the Cu:Sn ratio of Cu$_6$Sn$_5$ is 1.2. The WQ (10^3 °C/s) sample produced Cu$_6$Sn$_5$ particles with average Cu and Sn concentrations of 54.4 and 45.6 at. pct, respectively, with a Cu:Sn ratio of 1.19 within the Cu$_6$Sn$_5$ (η′) single phase region. Figures 5(a) through (d) illustrate the often observed formation of the Cu$_6$Sn$_5$ particles on the surfaces of the Cu$_x$Al$_y$ particles in the WQ (10^3 °C/s) sample, with the EDS maps (Figures 5(c) and (d)) qualitatively displaying the Cu and Sn content of the Cu$_6$Sn$_5$ particles in the WQ sample.

The aspect ratios of the Cu$_6$Sn$_5$ particles within the DSC cooled samples (Table I) ranged from 1.5 to 2.0, displaying the tendency of Cu$_6$Sn$_5$ to form large, faceted, hollow rods along the [0001] direction.[24] When considering the formation of the Cu$_6$Sn$_5$ phase from the ternary eutectic temperature (Figure 1(d)), the observed 281 K to 284 K (8 °C to 11 °C) undercooling within the DSC and WQ samples would have been sufficient to promote the formation of metastable proeutectic Cu$_6$Sn$_5$. Given the slow cooling rates of the DSC samples, coarsening of primary Cu$_6$Sn$_5$ would also have been likely, in agreement with the room temperature DSC microstructures. In comparison to the large
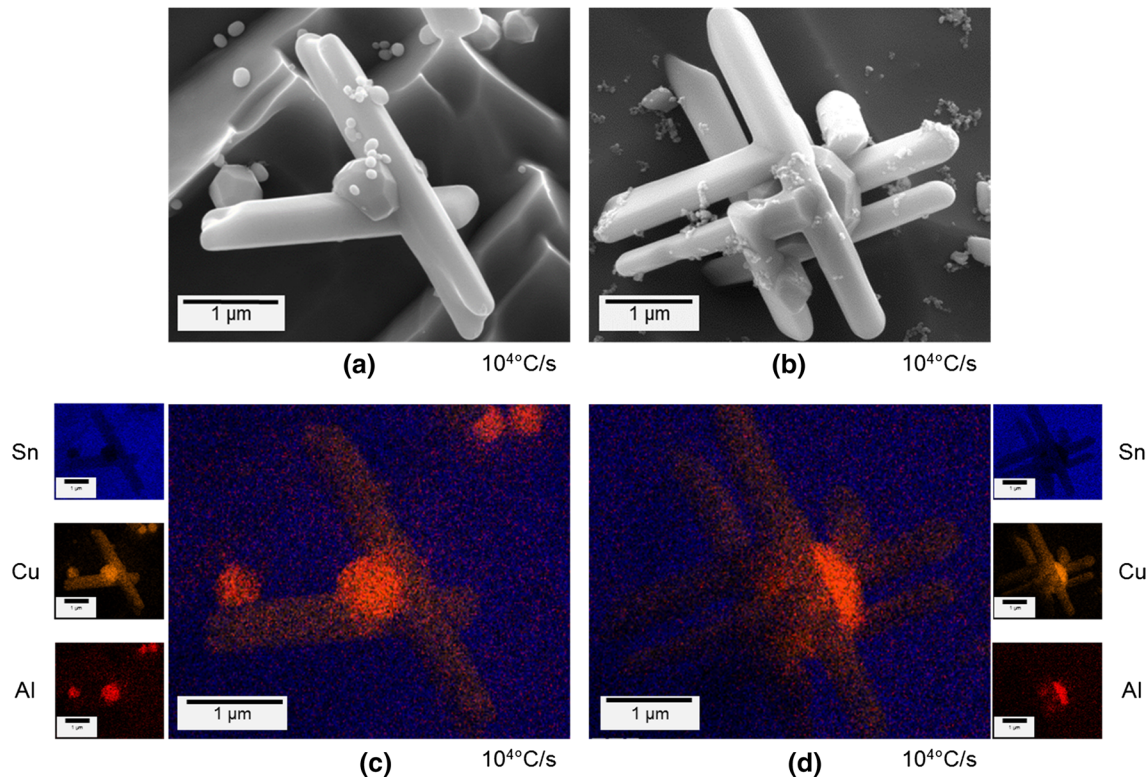
Fig. 8—(a) and (b) SEM SE images of regions of the Sn-2.59Cu-0.43Al at. pct DA (10^4 °C/s) sample after deep etching to reveal the 3-D structure of the IMC within the alloy. (c) and (d) SEM EDS map scans of the 3-D structure of the Sn-2.59Cu-0.43Al at. pct DA sample. Association between the Cu_6Sn_5 and Cu_xAl_y particle phases can be seen. (Color figures available online.).

primary Cu_6Sn_5 formation seen within the DSC samples, the Cu_6Sn_5 particles within the WQ (10^3 °C/s) sample were more equiaxed with an aspect ratio of 1.3. The Cu_6Sn_5 particles morphologies observed in the WQ sample using 2-D cross sections and 3-D deep etching (Figures 3(e) through (g) and Figures 5(a) through (d)) were comparable: small, nonfaceted, and nonhollow particle morphologies were observed, in contrast to the hollow, rod-like Cu_6Sn_5 particles produced in DSC cooling treatments. There were few instances of primary, faceted Cu_6Sn_5 particle formation noted in the WQ sample (see Figure 5(c)). In that case, the combination of low excess Cu in the liquid after formation of the Cu_xAl_y phase (0.59 at. pct) and a faster cooling rate (as compared to the DSC samples) likely resulted in limited growth of the Cu_6Sn_5 phase. The faster cooling rate of the WQ sample (10^3 °C/s) would have reduced the overall time in the liquid state when Cu_6Sn_5 was stable, leaving little time for Cu_6Sn_5 to coarsen and thus resulting in the small particle size observed in the sample (0.59 ± 0.05 μm), as compared to the DSC samples. The small, cylindrical Cu_6Sn_5 particles seen in the deep etched sample in Figures 5(a) and (b) support this hypothesis.

B. DA Sample: Composition #2 (Sn-2.59Cu-0.43Al at. pct)

Only one cooling rate (10^4 °C/s) was examined for this alloy as determined by the drip atomization process. The

DA sample contained a three-phase microstructure of Cu_xAl_y, Cu_6Sn_5 IMC, and β-Sn, as predicted from the solidification path for composition #2 (Figure 1(e)). The DA particle data for Cu_xAl_y and Cu_6Sn_5 phases can be found in Table I, while the compositional data for the two IMC phases can be found in Table II. The DA sample readily displayed association between Cu_6Sn_5 IMC and the Cu_xAl_y particles. It can be seen from the micrographs in Figures 7(a) through (c) that a majority of the Cu_6Sn_5 formed as rods, which appear to have nucleated on faceted Cu_xAl_y IMC particles, likely with the orientation relationship $(1\bar{2}10)_{Cu_6Sn_5} \parallel (10\bar{1})_{Cu_9Al_4}$ and $[0001]_{Cu_6Sn_5} \parallel [111]_{Cu_9Al_4}$, identified in References 5 and 6. The parallel rods shown in Figure 7(b) and in the 3-D deep etched micrographs, the EDS map scans of the DA sample in Figures 8(a) through (d), and the approximately 90 deg angles of Cu_6Sn_5 rod intersections (Figure 8(b)) are consistent with growth along the [0001] direction, following nucleation and growth on the $(10\bar{1})$ surfaces of Cu_xAl_y particles. More analysis is needed to identify the specific orientation relationships observed here for comparison with those observed previously.[5,6]

The Cu_xAl_y IMC average particle size in the DA sample (10^4 °C/s) was measured at 0.5 ± 0.2 μm. As shown in Figure 9(a), the Cu_xAl_y particle distribution ranges from 0.02 to 2.3 μm and possibly shows a slightly bimodal trend, with a small peak in the distribution at
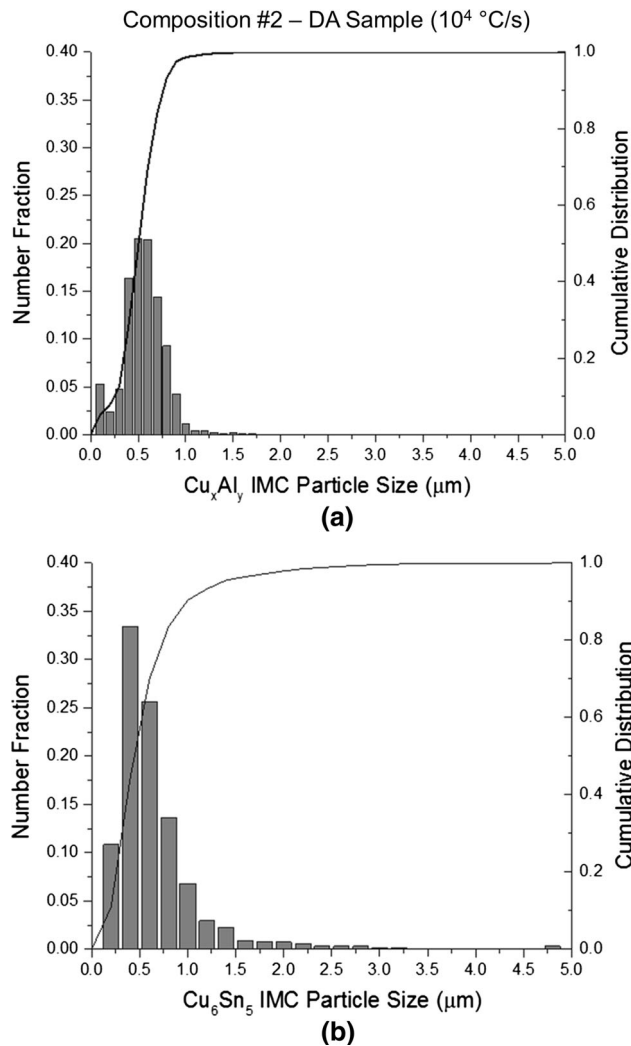
Composition #2 – DA Sample (10^4 °C/s)

(a)

(b)

Fig. 9—IMC particle size distributions for the Sn-2.59Cu-0.43Al at. pct DA (10^4 °C/s) sample for the (*a*) Cu$_x$Al$_y$ IMC particle phase and (*b*) the Cu$_6$Sn$_5$ IMC particle phase. The y-axis shows the number fraction of particles (bars, left axes) as well as the cumulative distribution function (lines, right axes). The x-axis plots the IMC particle size from 0 to 5 μm.

approximately 0.1 μm and a larger peak at the average value of approximately 0.5 μm. The measured volume fraction of Cu$_x$Al$_y$ IMC was 0.6 $\pm$ 0.1 pct, which is a value that matches the calculated theoretical volume fraction of 0.59 pct for the Sn-2.59Cu-0.43Al at. pct sample composition. The EDS measurements (Table II) taken from the 3-D deep etched DA sample revealed Cu and Al concentrations at an average of 67.7 and 31.9 at. pct, respectively. The qualitative EDS map scans shown in Figures 8(c) and (d) show the distribution of Sn, Cu, and Al within the DA sample microstructure and the spatial relationship between the two IMC phases, Cu$_x$Al$_y$ and Cu$_6$Sn$_5$. No indications of ternary-β phase decomposition were observed within the DA sample. The measured average Cu$_x$Al$_y$ composition places the Cu$_x$Al$_y$ particles within the DA sample in the Cu$_9$Al$_4$ (γ_1) phase.[12] The solidification path (Figure 1(e)) for the DA alloy predicts a three-phase microstructure of

β-Sn, Cu$_6$Sn$_5$ (η'), and Cu$_{33}$Al$_{17}$ (δ) at room temperature. This nonequilibrium prediction conflicts with the measured EDS composition of the Cu$_x$Al$_y$ particles within the sample, but as noted, the exact phase boundary and existence of a two-phase region between the Cu$_9$Al$_4$ and Cu$_{33}$Al$_{17}$ phases within the binary diagram is still under debate.[12]

The average Cu$_6$Sn$_5$ IMC particle size was measured at 0.6 $\pm$ 0.3 μm, with an average aspect ratio of 1.8, reflecting the elongated Cu$_6$Sn$_5$ particle morphology. The particle size distribution for the Cu$_6$Sn$_5$ phase within the DA (10^4 °C/s) sample can be seen in Figure 9(b) and ranged from 0.04 to 4.8 μm. The average Cu$_6$Sn$_5$ particle volume fraction within the DA sample was measured at 1.2 $\pm$ 0.2 pct, matching well with the theoretical volume fraction of Cu$_6$Sn$_5$ calculated for the Sn-2.59Cu-0.43Al at. pct sample composition of 1.22 pct. The EDS measurements regarding Cu$_6$Sn$_5$ composition were taken from the 3-D deep etched DA sample and produced averaged Cu and Sn concentrations of 60.1 and 39.9 at. pct, respectively. This resulted in a Cu:Sn ratio of 1.5, which is higher than the Cu:Sn ratio of Cu$_6$Sn$_5$ of 1.2. This alloy composition is within the Cu$_3$Sn (ε) + Cu$_6$Sn$_5$ (η') two-phase field, a result that does not match the single-phase particles seen within the microstructure. The measured Cu$_6$Sn$_5$ composition is approximately 3.5 at. pct from the lower bound of the Cu$_6$Sn$_5$ (η') single-phase region. It is possible, given the small particle size of the Cu$_6$Sn$_5$ phase (0.55 μm), that some scattering within the measurements occurred and that the measurements were rich in Cu due to surrounding Cu$_x$Al$_y$ particles.

The faceted, needle-like morphology of the Cu$_6$Sn$_5$ phase within the DA sample indicates lateral, screw dislocation-assisted growth of Cu$_6$Sn$_5$ prior to the ternary eutectic, previously described by Frear *et al.* as the mechanism for primary Cu$_6$Sn$_5$ needle growth.[24] When eliminating the formation of the ternary-β phase (Figure 1(e)), the Cu$_6$Sn$_5$ (η) phase is found to form prior to the ternary eutectic at approximately 513 K (240 °C). The rapid cooling rate (10^4 °C/s) of the DA sample likely restricted the overall size of the Cu$_6$Sn$_5$ (0.6 $\pm$ 0.3 μm), while the likelihood of primary Cu$_6$Sn$_5$ particle growth under nonequilibrium conditions resulted in the faceted Cu$_6$Sn$_5$ rods observed within the sample. In contrast, the DSC samples with composition #1, which were predicted to require undercooling to support the formation of primary Cu$_6$Sn$_5$, displayed coarsened, faceted Cu$_6$Sn$_5$ particles with hollow cores. Frear *et al.* examined the formation of hollow Cu$_6$Sn$_5$ rods within Sn-Pb solder joints and concluded that the hollowing process occurred due to low Cu concentrations in the liquid. The liquid, having been depleted of Cu during primary Cu$_6$Sn$_5$ formation, would begin to preferentially dissolve the centers of the Cu$_6$Sn$_5$ rods due to the high energy of the screw dislocation cores around which the rods formed.[24] Hollow Cu$_6$Sn$_5$ particles were observed in the DSC samples, which were likely produced due to ample time in the liquid state and low Cu concentration in the liquid (0.6 at. pct after Cu$_x$Al$_y$ formation). Conversely, only the beginnings of the

MSR 5m/s - Composition #3
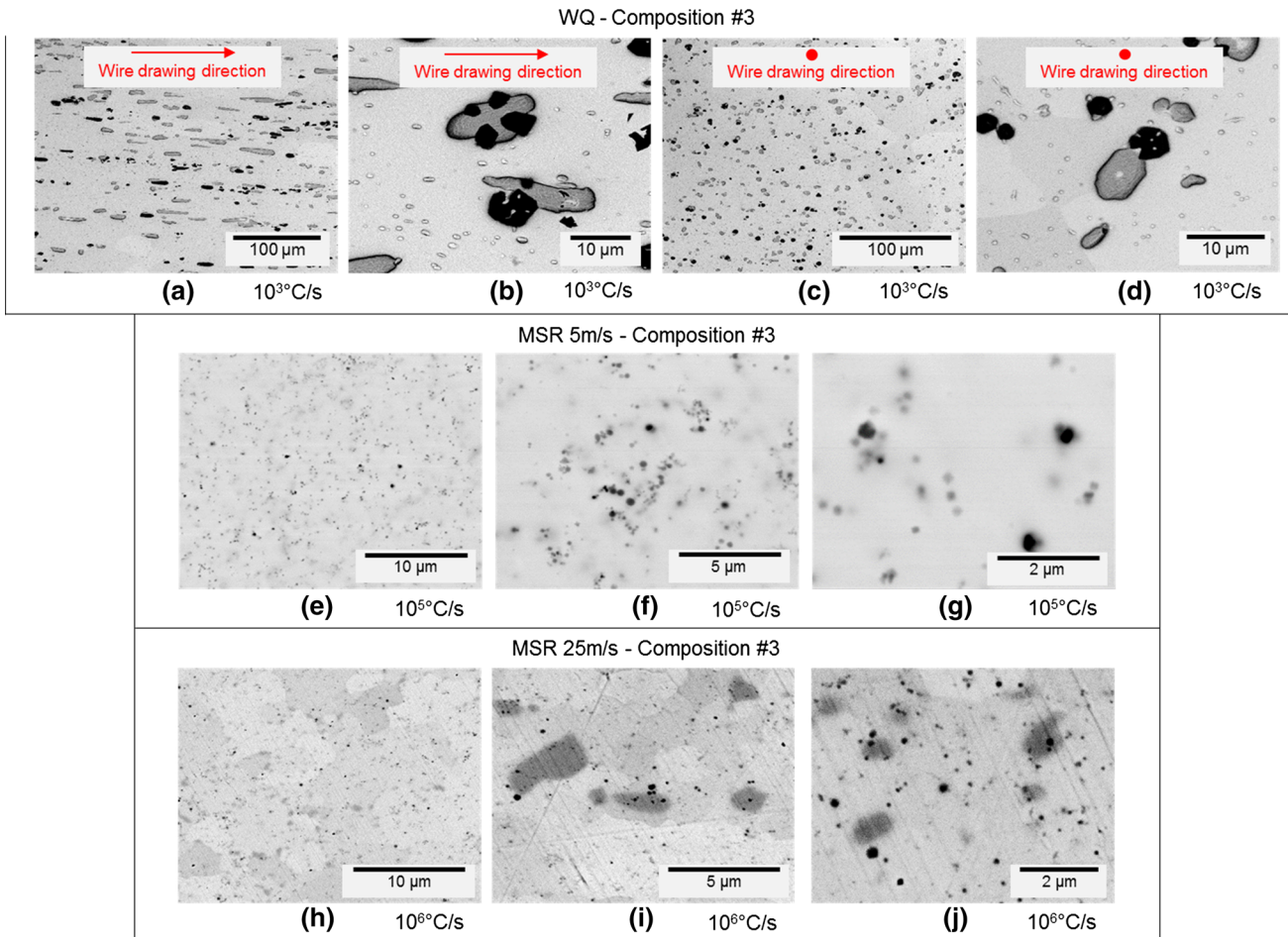
MSR 25m/s - Composition #3

Fig. 10—BSE SEM micrographs of the solder microstructure for Sn-5.39Cu-1.69Al at. pct samples, (a) through (d) WQ (10^3 °C/s) sample, (e) through (g) 5-m/s MSR (10^5 °C/s) sample, and (h) through (j) 25-m/s MSR (10^6 °C/s) sample. The black contrast particles are Cu_xAl_y IMC, the dark gray contrast particles and areas are Cu_6Sn_5 IMC, and the light gray matrix is β-Sn. (Color figures available online.).

dislocation core hollowing process were observed at the tips of the Cu_6Sn_5 needles in the DA sample (Figure 8(a)). The short time spent in the liquid state during DA and the higher Cu concentration in the liquid (1.7 at. pct after Cu_xAl_y formation) likely limited the progression of the core hollowing process within the DA sample.

C. WQ and MSR Samples: Composition #3 (Sn-5.39Cu-1.69Al at. pct)

The composition #3 WQ (10^3 °C/s) and MSR samples, 5 m/s (10^5 °C/s) and 25 m/s (10^6 °C/s), produced three-phase microstructures of β-Sn, Cu_6Sn_5, and Cu_xAl_y within the as-solidified samples, as predicted by the alloy's solidification path (Figure 1(f)). Micrographs of the 2-D cross sections from the WQ and MSR samples can be seen in Figures 10(a) through (j), and the 3-D deep etched images of the three samples can be seen in Figures 11(a) through (f). Particle size, distribution, volume fraction, and composition data can be found in Tables I and II. Measurements of the compositions of the Cu_xAl_y phase within the MSR samples were not performed due to the small size of the IMC particles.

The average Cu_xAl_y particle size of the WQ (10^3 °C/s) sample was 3.6 $\pm$ 2.0 μm. The average Cu_xAl_y particle sizes for both MSR cooling rates 5 m/s (10^5 °C/s) and 25 m/s (10^6 °C/s) were 0.1 $\pm$ 0.1 μm. The similarities between the Cu_xAl_y particle size measurements for the two MSR samples indicate a possible lower limit to the apparent cooling rate induced refinement of the Cu_xAl_y phase. Additionally, the volume fractions measured for the Cu_xAl_y phase within the 2-D cross sections of the MSR samples agree well with the theoretical volume fraction calculation for the phase based on the alloy composition. The volume fractions of Cu_xAl_y particles within the WQ (10^3 °C/s), 5 m/s (10^5 °C/s) MSR, and 25 m/s (10^6 °C/s) MSR cooling rate samples were measured at 2.0 $\pm$ 0.5, 2.1 $\pm$ 1.3, and 2.3 $\pm$ 0.6 pct, respectively, which all agree well with the theoretical volume fraction calculation of 2.39 pct. Comparison of the Cu_xAl_y particle size distributions for the WQ and MSR samples can be seen Figures 12(a) through (c). The distributions ranged from 1 to 11 μm in the WQ (10^3 °C/s) sample to 0.01 to 1 μm for both MSR samples (10^5 and 10^6 °C/s).

The average Cu_xAl_y compositions within the WQ (10^3 °C/s) sample were 66.8 at. pct Cu and 31.6 at. pct Al, (see Table II), corresponding to the Cu_9Al_4 (γ_1)
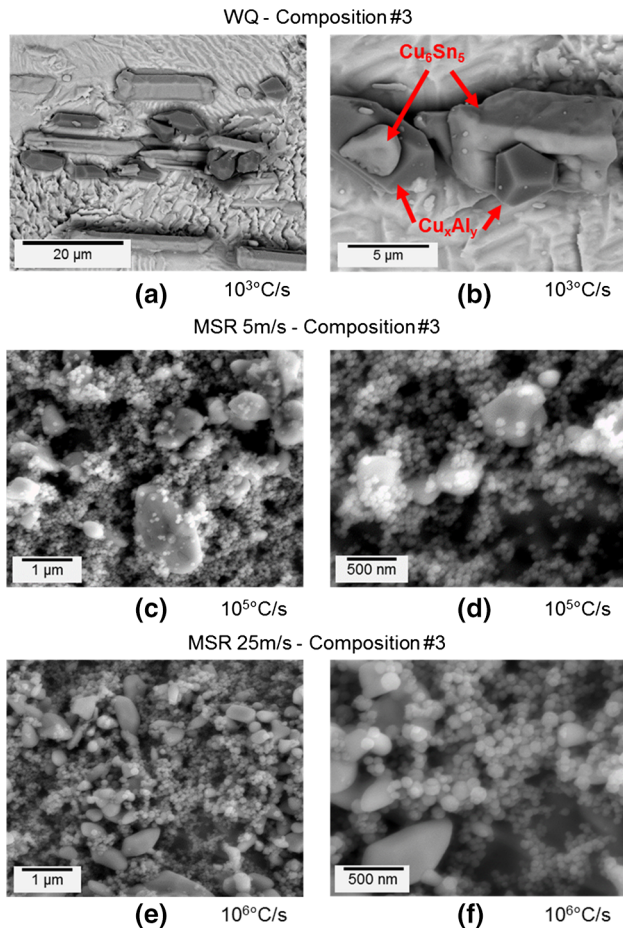
WQ - Composition #3

(a) 10³°C/s

(b) 10³°C/s

Cu₆Sn₅

CuₓAlᵧ

MSR 5m/s - Composition #3

(c) 10⁵°C/s

(d) 10⁵°C/s

MSR 25m/s - Composition #3

(e) 10⁶°C/s

(f) 10⁶°C/s

Fig. 11—SEM (*a*) and (*b*) BSE images, (*c*) through (*f*) SE images of the Sn-5.39Cu-1.69Al at. pct samples after deep etching to reveal the 3-D structure of the IMC within the alloy. (a) and (b) WQ (10^3 °C/s) sample, (c) and (d) 5-m/s MSR (10^5 °C/s) sample, and (e) and (f) 25-m/s MSR (10^6 °C/s) sample. Association between the Cu_6Sn_5 (light gray) and Cu_xAl_y (dark gray) particle phases can be seen in (a) and (b). Extreme refinement of the IMC can be seen in (c) through (f). (Color figures available online.).

phase.[12] The predicted phases at room temperature within the alloy included β-Sn, Cu_6Sn_5 (η'), and $Cu_{33}Al_{17}$ (δ) (Figure 1(f)). The solidification path omitting the ternary-β phase predicted the stability of the $Cu_{33}Al_{17}$ phase down to room temperature and the formation of the Cu_6Sn_5 (η) phase beginning at approximately 540 K (267 °C), prior to the ternary eutectic transformation. Comparison of the longitudinal and transverse wire drawing directions of the WQ (10^3 °C/s) sample (Figures 10(a)–(d)) revealed the elongation of the IMC particles in the wire drawing direction, a microstructure not observed within the wire-drawn composition #1 WQ (10^3 °C/s) sample. The micrographs in Figures 10(b) and (d) also show Cu_xAl_y particles with isolated pockets of Sn, a phenomenon that was noted throughout the WQ sample, possibly caused by the decomposition of the ternary-β phase during solidification. Isolated Sn pockets were also observed in the EDS qualitative map shown in Figure 13(a). Figure 13(b) shows a qualitative EDS map of an area of deep-etched WQ (10^3 °C/s) sample where the correlations between
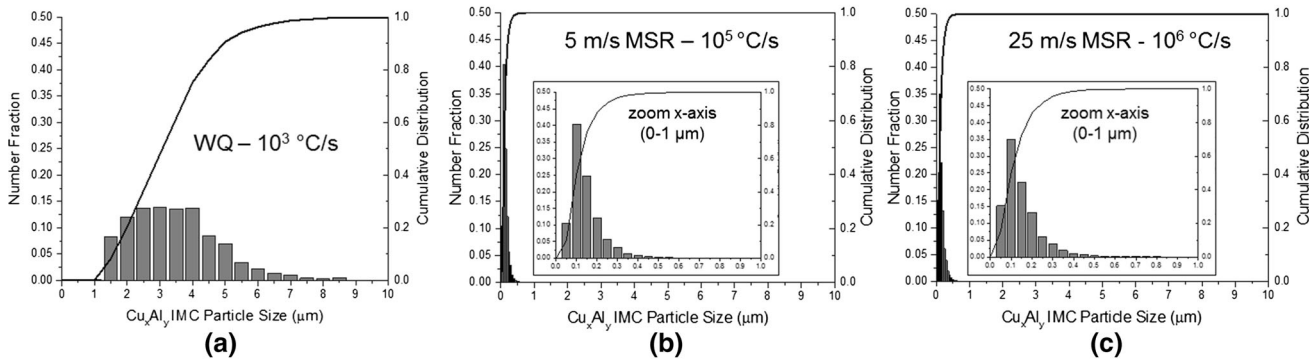
the distributions of Sn, Cu, and Al are used to identify the individual phases.

The average Cu_6Sn_5 particle sizes for the WQ (10^3 °C/s), 5 m/s MSR (10^5 °C/s), and 25 m/s MSR (10^6 °C/s) samples were measured at 2.5 ± 2.0, 0.5 ± 0.4, and 0.3 ± 0.2 μm, respectively. The particle size distributions for the Cu_6Sn_5 IMC within the three Sn-5.39Cu-1.69Al at. pct samples seen in Figures 12(d) through (f) narrow with the increase in cooling rate, from 0.2 to 8.9 μm in the WQ sample, 0.05 to 2.7 μm in the 5-m/s MSR sample, and 0.03 to 2.4 μm in the 25-m/s sample. The measured aspect ratios for the samples range from 1.5 to 1.6, all relatively similar, despite the morphology differences between the WQ and MSR samples. The volume fractions of the Cu_6Sn_5 IMC within the three samples were measured as 2.2 ± 0.6 pct for the WQ sample, 2.1 ± 0.6 pct for the 5-m/s MSR sample, and 1.7 ± 0.6 pct for the 25-m/s MSR sample, as compared to the 1.90 pct theoretical volume fraction for this alloy composition. The EDS measurements of the Cu_6Sn_5 phase within the WQ sample revealed concentrations of 51.9 at. pct Cu and 47.5 at. pct Sn, which is a composition within the Cu_6Sn_5 (η') + β-Sn two phase field (see Table II). These Cu and Sn concentrations yield a Cu:Sn ratio of 1.1, as compared to the Cu:Sn ratio of the stoichiometric Cu_6Sn_5 phase of 1.2. The high Sn concentration in the Cu_6Sn_5 particle may be due to the acquired signal contributed by the surrounding Sn matrix phase. The range of Cu_6Sn_5 IMC compositions within the deep-etched 5-m/s and 25-m/s MSR microstructures (10^5 and 10^6 °C/s) via EDS were 42.1–46.8 at. pct Cu, 43.7–47.6 at. pct Sn, and 9.5–10.3 at. pct Al. This result was unexpected, and it is possible that the Al concentration is attributed to the measurements from the surrounding Cu_xAl_y phase and/or Cu_xAl_y particles entrapped within the Cu_6Sn_5 particles (as seen in Figures 10(i) and (j)). This ternary composition could also indicate incomplete decomposition of the ternary-β phase in the solid state due to the high solidification rates within the samples.

The WQ sample displayed faceted Cu_6Sn_5 particle formation, with some particles displaying the hollow core morphology (Figures 10(d) and 11(a)). Given that Cu_6Sn_5 is predicted to form below approximately 540 K (267 °C), primary, faceted Cu_6Sn_5 particles would be expected to appear within the room temperature microstructure. The Cu_6Sn_5 particles appear to nucleate on the Cu_xAl_y particles, as seen in Figure 10(b). This type of configuration suggests a possible epitaxial orientation relationship between Cu_6Sn_5 and Cu_xAl_y, as reported in References 5 and 6, but it is not as pronounced as observed in the DA morphology. The only morphology of Cu_6Sn_5 particles observed within the WQ sample was large, faceted rods, with no bimodal particle size distribution observed.

The cross sections of the MSR samples shown in Figures 10(e) through (j) show the distributions and morphologies of the Cu_xAl_y and Cu_6Sn_5 phases for the two different cooling rates. Regions containing large, elliptical, nonfaceted Cu_6Sn_5 particles were noted throughout the MSR samples (Figures 10(i) through (j)), along with regions containing significantly smaller,
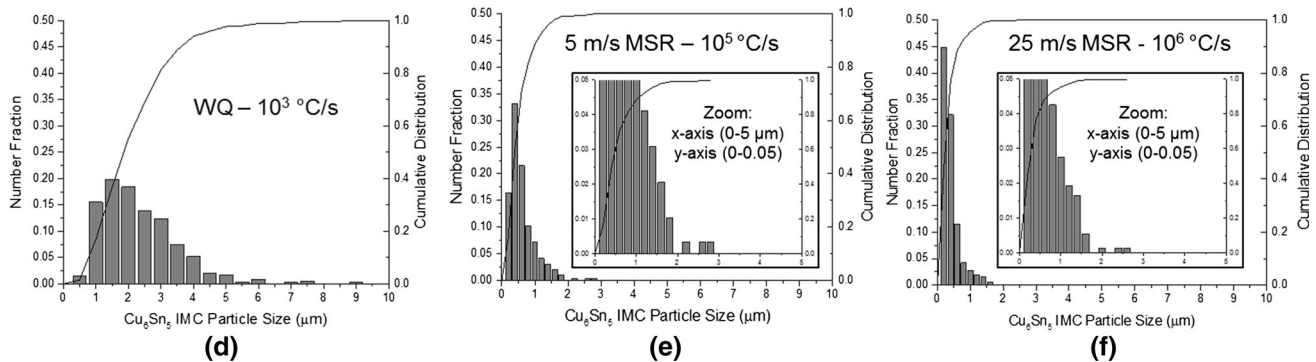
Fig. 12—IMC particle size distributions for the Sn-5.39Cu-1.69Al at. pct samples for the (*a*) through (*c*) Cu_xAl_y IMC particles within the WQ (10^3 °C/s), 5-m/s MSR (10^5 °C/s), and 25-m/s MSR (10^6 °C/s), respectively, and (*d*) through (*f*) the Cu_6Sn_5 IMC particles within the WQ (10^3 °C/s), 5-m/s MSR (10^5 °C/s), and 25-m/s MSR (10^6 °C/s), respectively. Insets are used in (b) and (c) to display the distribution of Cu_xAl_y within the MSR samples from 0 to 1 μm, and in (e) and (f) to display the trailing ends of each Cu_6Sn_5 distribution.

nonfaceted particles. The morphological transition of the Cu_6Sn_5 from faceted rods in the WQ sample to nonfaceted elliptical particles with a bimodal particle size distribution in the MSR samples is likely due to the high cooling rates for the MSR samples, 10^5 and 10^6 °C/s. Despite the remaining Cu in the liquid expected after Cu_xAl_y formation (2.1 at. pct Cu), the short time in the liquid state during Cu_6Sn_5 formation and particle coarsening precluded the transition to faceted rods. The deep-etched MSR samples shown in Figures 11(c) through (f) also displayed bimodal IMC particle distributions, with some relatively large particles and many others that had particle sizes on the nanoscale. Due to their small particle sizes, compositional measurements on the nanoscale particle phase could not be performed to distinguish Cu_xAl_y from Cu_6Sn_5. Given the accuracy of the measured volume fractions of the Cu_xAl_y phase within the MSR samples and the predicted high trans-formation temperature of the $Cu_{33}Al_{17}$ phase, first solidifying at ~813 K (~540 °C) and completely trans-formed by 573 K (~300 °C) (Figure 1(f)), it is unlikely that all of these nanoscale particles are that of the Cu_xAl_y phase. When further referencing the solidifica-tion path without the ternary-β phase in Figure 1(f), it can be seen that the mole fraction of the Cu_6Sn_5 phase more than doubles at the alloy's eutectic transformation temperature. Given this increase in Cu_6Sn_5 phase fraction at the eutectic temperature and the extremely

rapid cooling rates of the MSR samples, it is likely that the nanoscale particles in Figures 11(d) and (f) are predominantly Cu_6Sn_5 formed from the eutectic trans-formation, but TEM analysis would be required for confirmation.

To summarize the IMC particle size measurements made for all compositions, the graphs in Figures 14(a) and (b) illustrate the overall refinement of the Cu_xAl_y and Cu_6Sn_5 particle sizes for the range of the applied cooling rate techniques. Figures 14(a) and (b) display the progression from the slowest controlled cooling at 0.017 °C/s to the fastest RSP method employed *via* melt spinning at a wheel speed of 25 m/s (estimated cooling rate of 10^6 °C/s), which resulted in an overall decrease in Cu_xAl_y and Cu_6Sn_5 particle sizes by approximately two orders of magnitude. These data illustrate the ability to manipulate the as-solidified particle sizes of the Cu_xAl_y and Cu_6Sn_5 IMC based solely on the chosen solidifica-tion method. Second, the data show that there is strong microstructural evidence for the Cu_6Sn_5 IMC particles nucleating on Cu_xAl_y particles only at intermediate cooling rates, as observed for the WQ and DA samples. Nevertheless, there is less direct (EDS reveals a high Al content in the apparent Cu_6Sn_5 particles) evidence in both MSR samples of Cu_6Sn_5 particles nucleating on (embedded, unseen) Cu_xAl_y particles, but the SEM resolution was not sufficient to observe this. In addition, faceted rod formation and the subsequent hollowing of
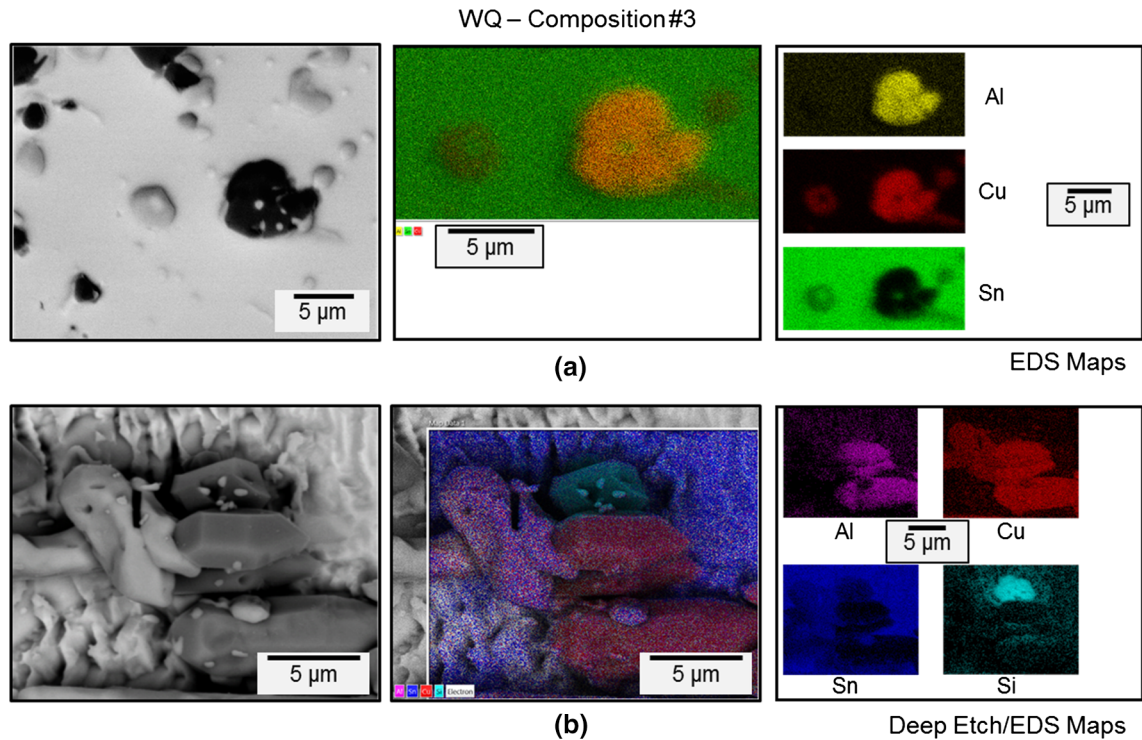
WQ – Composition #3

(a) ... EDS Maps

(b) ... Deep Etch/EDS Maps

Fig. 13—SEM BSE images and EDS map scans of regions of Sn-5.39Cu-0.86Al at. pct WQ (10^3 °C/s) sample (*a*) 2-D cross section and (*b*) SE images after deep etching to reveal the 3-D structure of the IMC within the alloy. Association between the Cu_6Sn_5 (light gray) and Cu_xAl_y (black) particle phases can be seen throughout the micrographs. Sn-entrapment within the Cu_xAl_y phase is also observed in (*a*). (Color figures available online.).

Cu_6Sn_5 rods is shown to depend on composition and cooling rate. For example, the slowly cooled DSC samples displayed faceted, hollow Cu_6Sn_5 due to low Cu concentrations in the liquid during solidification and the slow cooling rate of the samples, while the WQ sample of the same composition displayed nonfaceted, nonhollow Cu_6Sn_5 particles with the increase in cooling rate, as outlined in Table I. The combination of these results suggests that a cooling rate regime utilizing water quenching to drip atomization (10^3 to 10^4 °C/s) is ideal to achieve IMC particle refinement while maintaining the Cu_xAl_y/Cu_6Sn_5 nucleant relationship during initial solidification from the melt. Finally, there appears to be little microstructural evidence for the presence of the ternary-β phase during solidification or for its decomposition at lower temperatures for the DSC cooled, DA, WQ, or MSR samples. (The specific instances of microstructures that suggested decomposition of the ternary-β phase were described here, but they were rare.) This result is in contrast to what was observed previously for WQ Sn-Ag-Cu-Al quaternary alloys,[2] suggesting that the ternary-β phase does not form within the ternary alloy composition ranges and cooling rates investigated here and may be unstable, in agreement with observations by Xian *et al.* for a different set of Sn-Cu-Al alloys.[5,6]

It is widely recognized that the Cu_6Sn_5 particle size distribution can be strongly affected by variations in β-Sn undercooling during alloy solidification. These often unpredictable and unrepeatable variations in β-Sn

undercooling can lead to increased Cu_6Sn_5 particle size with increased β-Sn undercooling.[25] In Part II of this study, the coarsening behavior of alloys during thermal reflow cycling between 293 K and 523 K (20 °C and 250 °C) for 1 to 5 cycles for the DA and 5-m/s MSR samples was examined. It was shown that the particle size of the Cu_xAl_y was essentially unaffected by the thermal cycling, displaying no signs of coarsening during reflow cycling. In contrast, the particle size distribution of the Cu_6Sn_5 phase at the slow cooling rates used in Part II during reflow cycling (10°C/min or 0.17°C/s) varied quite significantly, corresponding to the large variations in β-Sn undercoolings observed. Such a large range in particle size distribution of the Cu_6Sn_5 phase was not observed in the samples from Part I of this study, and it is because of this that the authors are confident that the changes in cooling rate are the dominating factor in the refinement of the as-solidified IMC microstructures. Additionally, the high diffusivity of Cu in Sn certainly means that these intermetallics could potentially change over time at room temperature.[25] Room temperature microstructural evolution has been reported for Cu_6Sn_5 in many different solder systems, but the authors have not observed any room temperature microstructural changes in regard to the Cu_xAl_y phase in this study and believe the phase to be quite stable at room temperature, especially considering the results from Part II of this study, where the particle size of the Cu_xAl_y was essentially unaffected by the thermal cycling to 523 K (250 °C).
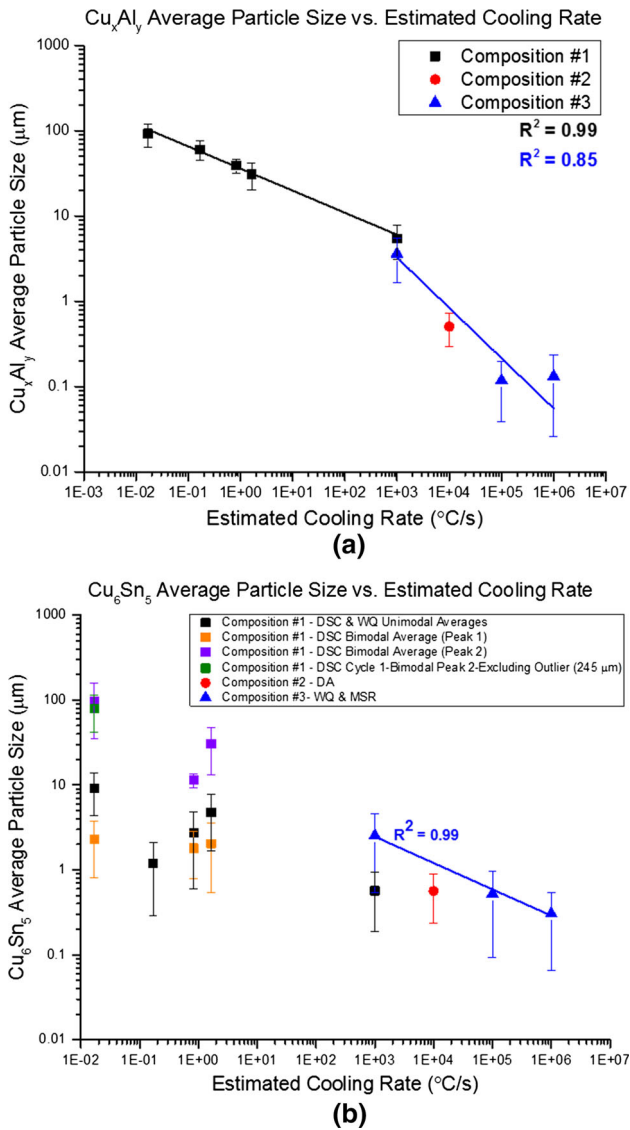
Fig. 14—Graph of (a) Cu_xAl_y and (b) Cu_6Sn_5 IMC average particle diameters *vs* applied estimated cooling rate for the three alloy compositions examined. In (b), the average unimodal and bimodal particle diameters for the DSC cooled samples are given. The linear fits shown in (a) and (b) portray the decreasing size of the Cu_xAl_y and Cu_6Sn_5 particles with applied cooling rate for the corresponding alloy compositions. (Color figures available online.).

IV. CONCLUSIONS

This article has shown that the Cu_xAl_y and Cu_6Sn_5 IMC particle formations within Sn-Cu-Al alloys are highly dependent on alloy composition and cooling rate. Through application of RSP methods, with cooling rates up to approximately 10^6 °C/s, the particle sizes and particle size distributions of the Cu_xAl_y and Cu_6Sn_5 IMC particle phases were refined well into the submicron range. For application of the fastest cooling rate of 10^6 °C/s, produced *via* melt spinning of composition #3 at a 25-m/s wheel speed, the average Cu_xAl_y IMC particle diameter was refined to 0.1 ± 0.1 μm, while the Cu_6Sn_5 particle size was refined to 0.3 ± 0.2 μm.

The morphology of the Cu_6Sn_5 phase within the Sn-Cu-Al solders was also manipulated *via* the use of RSP. A transition in the Cu_6Sn_5 morphology from faceted rods to nonfaceted, more equiaxed particles occurred with increased cooling rates, with the cooling rate threshold dependent on composition, *i.e.,* dependent on available Cu content within the liquid during cooling and, therefore, on the formation temperature of the Cu_6Sn_5 phase (predicted in Figures 1(d) through (f)). This transition for composition #1 occurred with increased cooling rate from DSC cooling (maximum of 1.65 °C/s) to WQ processing (10^3 °C/s). When considering composition #1, the Cu_6Sn_5 phase was not predicted to form until the ternary eutectic reaction at ~500 K (~227 °C) (Figure 1(d)). Due to the low Cu content in the liquid (0.59 at. pct) after the complete formation of the Cu_xAl_y phase, the formation of any primary Cu_6Sn_5 within composition #1 would have required undercooling below the ternary reaction. The cooling rate threshold for composition #1 was therefore lower than that of composition #3, due to the latter alloy's increased content of Cu in the liquid (2.1 at. pct Cu), where formation of the Cu_6Sn_5 phase was predicted to begin at ~540 K (~267 °C) (Figure 1(f)). The faceted to nonfaceted transition in Cu_6Sn_5 was observed within composition #3 between the WQ cooling rate (10^3 °C/s) and the MSR processing at 10^5 °C/s. The DA sample (composition #2, 10^4 °C/s) displayed faceted Cu_6Sn_5 formation, but there were no other tested cooling rates for this sample composition with which to compare.

Finally, the room temperature microstructures revealed little evidence of ternary-β phase formation during solidification, or its decomposition at lower temperatures, within all of the current ternary alloy compositions and cooling rates. (The few instances of microstructures that suggested possible decomposition of the ternary-β phase were described, but it is noted that these instances were rare.) Based on these observations, solidification path predictions omitting the ternary-β phase formation were calculated and presented. The predicted solidification paths all displayed the stabilization of the $Cu_{33}Al_{17}$ (δ) phase down to room temperature, with the Cu_6Sn_5 (η) phase forming at various temperatures: at the eutectic temperature [~500 K (~227 °C)] for composition #1, but higher than the ternary eutectic for the composition #2 [at ~513 K (~240 °C)] and composition #3 [at ~540 K (~267 °C)]. This is in contrast to what was observed previously for WQ Sn-Ag-Cu-Al quaternary alloys, where the microstructures showed multiple, interconnected IMC phases within single particles.[2] In this study, the absence of such structures suggests that the ternary-β phase did not form within the ternary alloy composition ranges and cooling rates investigated here and may, in fact, be unstable, in agreement with observations by Xian *et al.* for a different set of Sn-Cu-Al alloys.[5,6] Continued research into the ranges of stability of the ternary-β phase should be explored *via* long-term isothermal annealing and quenching experiments on select Sn-rich Sn-Cu-Al ternary alloys.

In general, these experiments show strong evidence for the nucleation of Cu_6Sn_5 on Cu_xAl_y particles at different cooling rates and compositions and, therefore, that

Cu_xAl_y particles can be effective nucleation agents when the average particle sizes decrease and size distributions of the IMCs narrow with increasing cooling rates. It was determined that to achieve a microstructure with both Cu_xAl_y and Cu_6Sn_5 IMC refinement and a maintained Cu_xAl_y/ Cu_6Sn_5 nucleant relationship, cooling rates within the range of water quenching to drip atomization (10^3–10^4 °C/s) are the most effective. The usefulness of these alloys in controlling microstructure evolution in solder interconnects will depend on the continued ability of the Cu_xAl_y particles to be effective nucleating agents for Cu_6Sn_5 during multiple reflow cycles. In Part II, the melting and solidification behaviors of the Sn-2.59Cu-0.43Al at. pct DA (10^4 °C/s) alloy and the Sn-5.39Cu-1.69Al at. pct 5 m/s (10^5 °C/s) MSR alloy were examined using DSC temperature cycling [293 K to 523 K (20 °C to 250 °C)] up to five reflow cycles to study the nucleation and coarsening behavior of the Cu_xAl_y and Cu_6Sn_5 IMC phases present within both alloys.[21]

REFERENCES

1. A.J. Boesenberg, I.E. Anderson, and J.L. Harringa: *J. Electron. Mater.*, 2012, vol. 41, pp. 1868–81.
2. K.N. Reeve, I.E. Anderson, and C.A. Handwerker: *J. Electron. Mater.*, 2015, vol. 44, pp. 842–66.
3. S.D. McDonald, K. Nogita, J. Read, T. Ventura, and T. Nishimura: *J. Electron. Mater.*, 2012, vol. 42, pp. 256–62.
4. K. Sweatman, T. Nishimura, S.D. McDonald, M. Whitewick, and K. Nogita: *SMT Mag.*, 2014, pp. 30-40.
5. J.W. Xian, S.A. Belyakov, T.B. Britton, and C.M. Gourlay: *J. Alloys Compd.*, 2015, vol. 619, pp. 345–55.
6. J.W. Xian, S.A. Belyakov, and C.M. Gourlay: *J. Electron. Mater.*, 2015, vol. 45, pp. 69–78.
7. C.S. Smith, W.E. Lindief, and W. Conn: *Trans. Am. Inst. Min. Metall. Eng.*, 1933, vol. 104, pp. 69–105.
8. G. Wasserman: *Metallwirtschaft*, 1934, vol. 13, pp. 133–39.
9. J.L. Murray: *Int. Met. Rev.*, 1985, vol. 30, pp. 211–33.
10. X.J. Liu, I. Ohnuma, R. Kainuma, and K. Ishida: *J. Alloys Compd.*, 1998, vol. 264, pp. 201–8.
11. H. Okamoto: *Desk Handbook: Phase Diagrams for Binary Alloys*, ASM International, Materials Park, 2000.
12. N. Ponweiser, C.L. Lengauer, and K.W. Richter: *Intermetallics*, 2011, vol. 19, pp. 1737–46.
13. S. Fürtauer, D. Li, D. Cupid, and H. Flandorfer: *Intermetallics*, 2013, vol. 34, pp. 142–7.
14. D. Li, P. Franke, S. Fürtauer, D. Cupid, and H. Flandorfer: *Intermetallics*, 2013, vol. 34, pp. 148–58.
15. J.S.L. Leach and G.V. Raynor: *Proc. R. Soc.*, 1954, vol. 224, pp. 251–9.
16. A.K. Chakrabarty and K.T. Jacob: *Int. J. Mater. Res.*, 2013, vol. 104, pp. 430–41.
17. A.K. Chakrabarty and K.T. Jacob: *J. Phase Equilibria Diffus.*, 2013, vol. 34, pp. 267–76.
18. D. Mirković, J. Gröbner, and R. Schmid-Fetzer: *Mater. Sci. Eng. A*, 2008, vol. 487, pp. 456–67.
19. W.J. Boettinger and J.H. Perepezko: in *Rapidly Solidified Cryst. Alloy.*, S.K. Das, B.H. Kear, and C.M. Adam, eds., The Metallurgical Society, Inc., Warrendale, PA, 1985, pp. 21–58.
20. S.A. Belyakov and C.M. Gourlay: *Acta Mater.*, 2014, vol. 71, pp. 56–68.
21. K.N. Reeve, S.M. Choquette, I.E. Anderson, and C.A. Handwerker: *Metall. Mater. Trans. A*, 2016, DOI:10.1007/S11661-016-3739-5.
22. L. Arnberg and S. Westman: *Acta Crystallogr. Sect. A*, 1978, vol. 34, pp. 399–404.
23. E.H. Kisi and J.D. Browne: *Acta Crystallogr. Sect. B*, 1991, vol. 47, pp. 835–43.
24. D. Frear, D. Grivas, and J.W. Morris, Jr: *J. Electron. Mater.*, 1987, vol. 16, pp. 181–86.
25. B.F. Dyson, T.R. Anthony, and D. Turnbull: *J. Appl. Phys.*, 1967, vol. 38, p. 3408.